

# **Nonlinear Analyses for Embedded Cracks Under Pressurized Thermal Shock: Comparisons with FAVOR and Weibull Stress Approaches**

# **Nonlinear Analyses for Embedded Cracks Under Pressurized Thermal Shock: Comparisons with FAVOR and Weibull Stress Approaches**

Manuscript Completed: August 2007

Date Published: February 2008

Prepared by  
B. Wasiluk<sup>1</sup>, X. Qian<sup>2</sup> and R.H. Dodds, Jr.<sup>1</sup>

<sup>1</sup>Department of Civil and Environmental Engineering  
University of Illinois at Urbana-Champaign  
205 N. Mathews Avenue  
Urbana, IL 61801

<sup>2</sup>Oak Ridge National Laboratory  
P.O. Box 2008  
Oak Ridge, TN 37831

S.N. Malik, NRC Project Manager

NRC Job Code Y6951

Office of Nuclear Regulatory Research

This page is intentionally blank.

# Nonlinear Analyses for Embedded Cracks Under Pressurized Thermal Shock: Comparisons with FAVOR and Weibull Stress Approaches

by

Bogdan Wasiluk, Xudong Qian and Robert H. Dodds Jr.

## Abstract

Thick-walled reactor pressure vessels (RPVs) can potentially experience rapid temperature and pressure changes under pressurized thermal shock (PTS) conditions. This work describes progress towards utilization of a Weibull stress approach for cleavage fracture assessment of RPVs subjected to PTS events. The Weibull stress approach couples the macroscopic crack driving force,  $J$  or  $K_I$ , with the local, crack-front conditions for cleavage characterized by the Weibull stress and requires realistic stress analyses. Extensive previous work focused on the conventional, linear-elastic stress-intensity factor (SIF),  $K_I$  values for flaws in RPVs. This study begins by comparing predictions of the macroscopic crack driving force ( $K_I$ ) made by the FAVOR (Fracture Analysis for Vessels – Oak Ridge) code with detailed, linear-elastic and elastic-plastic finite element analyses for circumferentially and axially embedded flaws located in a representative RPV and subjected to two well characterized transients, denoted here as transients A and B. These solutions provide needed benchmarks for future efforts to approximate the nonlinear material response near the crack front through a simpler, linear-elastic  $K_I$ - $T$  stress field imposed on a 2-D, small-scale yielding configuration. The postulated loadings considered here include a critical thermal transient with a small change of internal pressure (Transient A) and a mild thermal transient concurrent with significant re-pressurization (Transient B). The RPV models employ ferritic steel for the base material and austenitic steel for the cladding; the combination leads to pronounced mismatches in both the mechanical and thermal properties. The SIF computed from the linear-elastic analyses show lower values than the  $K_I$ -solutions obtained from the elastic-plastic analyses. Based on previous research for the Weibull stress approach applied to through-crack fracture specimens, the current study concludes with proposals for refined and simplified engineering procedures, as well as a  $K_I$ - $T$  stress methodology, for defect assessments of curved, embedded flaws in RPVs under PTS conditions.

## Paperwork Reduction Act Statement

This report does not contain information collection requirements and, therefore, is not subject to the requirements of the Paperwork Reduction Act of 1995 (44 U.S. C. 3501 et seq.).

This page is intentionally blank.

## Foreword

---

The U.S. Nuclear Regulatory Commission (NRC) has analyzed the potential for cleavage fracture in reactor pressure vessels (RPVs) under pressurized thermal shock (PTS) loading, which may cause sudden failure without prior or extensive deformation. These analyses have been performed using the NRC-supported Fracture Analysis of Vessels – Oak Ridge (FAVOR) computer code developed and maintained by the Oak Ridge National Laboratory (ORNL), which calculates crack opening (mode-I) linear-elastic stress-intensity factors ( $K_I$ ) for three-dimensional (3-D) embedded or surface cracks in the wall of an RPV. In contrast to the linear-elastic solutions generated using the FAVOR code, during a real fracture event, crack propagation would be accompanied by some level of plastic deformation at the crack front that would redistribute the stresses calculated by linear-elastic fracture mechanics (LEFM) theory to adjacent material. Use of LEFM analysis is simpler and computationally expedient but under certain loading conditions and crack sizes leads to less accurate values of the crack driving force ( $K_I$ ) as predicted by the elastic-plastic fracture mechanics (EPFM) analyses presented in this report. This report describes a method for using EPFM analyses to improve accuracy in the LEFM-based FAVOR code predictions.

This report describes 3-D elastic-plastic analyses for selected RPVs under severe PTS transients and provides a detailed procedure to benchmark probabilistic fracture mechanics schemes for implementation in an EPFM-based modular structural integrity evaluation code. Also, this study improves the understanding of failure assessment procedures for embedded cracks in RPVs under PTS events by (1) comparing the prediction of crack driving force ( $K_I$ ) values via the linear-elastic FAVOR code and the detailed, elastic-plastic, 3-D finite element analyses and (2) discussing in depth the three detailed assessment procedures and providing an illustrative example involving postulated PTS transients.

The approach described in this report demonstrates the analyses used to evaluate reactor vessel's resistance to cleavage fracture, as implemented in the FAVOR code, is generally conservative. For future applications of the FAVOR code to components in situations that exhibit greater plasticity (e.g., piping and thin-walled sections), this report describes a method for calculating the crack driving force with greater accuracy.

---

Jennifer L. Uhle, Director  
Division of Engineering  
Office of Nuclear Regulatory Research  
U.S. Nuclear Regulatory Commission

This page is intentionally blank.

# Contents

---

Abstract .....	iii
Foreword .....	v
Contents .....	vii
Figures .....	ix
Tables .....	xi
Executive Summary .....	xiii
Acknowledgements .....	xv
Acronyms .....	xvii
1. Introduction .....	1
2. Computational Procedures and the Weibull Stress Model .....	5
2.1 FAVOR Code .....	5
2.2 Computation of $J$ Integral for Mechanical and Thermal Loading .....	5
2.3 Weibull Stress Model .....	7
3. Finite Element Modeling .....	11
3.1 RPV with Embedded Flaws .....	11
3.2 Material Properties of the Base and Cladding Steels .....	11
3.3 PTS Transients .....	14
3.4 Finite Element Models .....	15
4. Crack Driving Forces for Two Transients .....	23
4.1 Transient A .....	23
4.2 Transient B .....	27
4.3 Plastic Material Response Under PTS .....	30
5. Weibull Stress Approach .....	33
5.1 Weibull Stress Values for RPVs Under PTS .....	33
5.2 Estimation of Weibull Stress Parameters .....	35

6.	Application of Local Approach to PTS Assessment .....	39
6.1	Complications for RPVs .....	39
6.2	A Refined Procedure for PTS Assessment .....	39
6.3	A Simplified Procedure for PTS Assessment .....	41
6.4	$K_I$ - $T$ Approximation for Nonlinear Crack-Front Fields .....	42
7.	Summary and Conclusions .....	47
	References .....	49
	Appendix A: Calibration of Weibull Stress Model.....	A-1
	Appendix B: Future Work .....	B-1
	Appendix C: Analytical Solutions for Thermal Induced $T$ -Stress .....	C-1

# Figures

---

1. Geometric configuration of: (a) a quarter symmetric model of a reactor pressure vessel; and (b) an embedded flaw in the wall of the RPV. ....	12
2. Uniaxial, true stress-logarithmic strain relationships for: (a) the vessel wall (ferritic) steel for the RPV; and (b) the austenitic stainless steel for the cladding. ....	13
3. Transient conditions: (a) Transient A cooling temperature; (b) Transient A internal pressure; (c) Transient B cooling temperature; and (d) Transient B internal pressure. Simple linear interpolations smooth these loading histories for input to the fracture analyses.....	17
4. Temperature variations over the wall thickness at time intervals of 5 minutes computed by the 1-D axisymmetric analysis in FAVOR for: (a) Transient A; and (b) Transient B. ....	18
5. Models using 8-node brick elements for RPV with a circumferentially embedded elliptical flaw (LEFM = Linear-Elastic Fracture Model; EPFM = Elastic-Plastic Fracture Model). ....	19
6. Models using 8-node brick elements for RPV with an axially embedded elliptical flaw (LEFM = Linear-Elastic Fracture Model; EPFM = Elastic-Plastic Fracture Model). ....	20
7. Models using 20-node brick elements for an RPV with a circumferentially embedded elliptical flaw: (a) for linear-elastic analysis; and (b) for elastic-plastic analysis (LEFM = Linear-Elastic Fracture Model; EPFM = Elastic-Plastic Fracture Model). ....	21
8. Models using 20-node brick elements for an RPV with an axially embedded elliptical flaw: (a) for linear-elastic analysis; and (b) for elastic-plastic analysis (LEFM = Linear-Elastic Fracture Model; EPFM = Elastic-Plastic Fracture Model). ....	22
9. $K_I$ -values along the crack front for Transient A (FE models using 8-node brick elements) with: (a) a circumferentially embedded flaw; and (b) an axially embedded flaw. ....	25
10. $K_I$ -time history for Transient A with: (a) a circumferentially embedded flaw using 8-node elements; (b) an axially embedded flaw using 8-node elements; (c) a circumferentially embedded flaw using 20-node elements; and (d) an axially embedded flaw using 20-node elements. ....	26
11. $K_I$ -time history for Transient B with: (a) a circumferentially embedded flaw using 8-node elements; (b) an axially embedded flaw using 8-node elements; (c) a circumferentially embedded flaw using 20-node elements; and (d) an axially embedded flaw using 20-node elements. ....	29
12. The fringe plot of Mises equivalent stress for Transient A imposed on an axially embedded flaw, computed using 20-node brick elements at $t = 18$ min. ....	31
13. Weibull stress variation over time history for an axially embedded flaw subjected to Transient A (20-node element model) with $\sigma_{eff} = \sigma_1$ and: (a) $\lambda = 1.5$ ; (b) $\lambda = 2.0$ ; (c) $\lambda = 2.5$ ; and (d) $\lambda = 2.7$ . ....	37
14. Weibull stress variation over time history for an axially embedded flaw subjected to Transient A (20-node element model) with $\sigma_{eff} = \sigma_H$ and: (a) $\lambda = 1.25$ ; (b) $\lambda = 1.5$ ; (c) $\lambda = 1.8$ ; and (d) $\lambda = 2.0$ . ....	44

- 15. (a) Evolution of constant  $C$  with  $K_I$ -values in SSY conditions; (b) variation of (SSY)  $\sigma_u$  with respect to time at  $P_{crit}$  along the embedded crack front under Transient A; (c) cumulative probability of failure for the axial flaw under Transient A; and (d) sensitivity of  $P_f$  (computed from Eq. 12) to  $\sigma_u$ -values for fixed  $\sigma_w$ -values. .... 45
- A1. Quadratic approximation of temperature variations over the wall thickness of an RPV under (a) transient A and (b) transient B. Comparison of the analytical solution and the FE analysis over the wall thickness of an RPV at  $t = 20$  min of transient A for (c)  $\sigma_{rr}$  and (d)  $\sigma_{\theta\theta}$ . .... A-4
- A2. Comparison of the  $T$ -stress values computed using the interaction integral including thermal loadings and those excluding thermal loadings for an RPV under (a) transient A; and (b) transient B.. .... A-5

## Tables

---

1. RPV and embedded elliptical flaw dimensions .....	14
--	----

This page is intentionally blank.

## Executive Summary

---

This work advances the understanding and numerical analysis procedures to predict the crack driving forces for embedded 3-D flaws in reactor pressure vessels (RPVs) subjected to pressurized thermal shock (PTS) events. A PTS event generates rapid cooling and significant changes in the internal pressure acting on an RPV. The decrease in temperature and the temperature gradients increase the probability of cleavage failure for ferritic steels in the wall of an RPV by localized loading along the crack front and by reducing the material fracture toughness. The statistical sampling of potential flaws contains a wide range of shapes, sizes, locations and orientations in the wall of an RPV, constructed using ferritic steels with complex thermal and mechanical properties. The potential for cleavage fracture in RPVs under PTS causes concern since sudden failure can occur without extensive, prior deformation. One developing, probabilistic method of integrity assessment for such RPVs correlates the macroscopic toughness-temperature relationship described by the Master Curve (as detailed in ASTM E-1921[29]) with the Weibull stress framework which characterizes the local, crack-front conditions through a scalar Weibull stress value. To compute the cumulative probability of fracture, this assessment approach requires a detailed, realistic stress analysis, which depends significantly on the geometry of the existing flaw, temperature-dependent material properties, and complex thermal gradients over the wall thickness.

In the past two decades, substantial research efforts [3-7] have generated comprehensive libraries of linear-elastic, stress-intensity weight functions for embedded or surface breaking flaws in RPVs subjected to combined thermal and mechanical loadings. The inherent assumption of linear-elastic behavior enables various superposition schemes to compute stress-intensity factors for real, 3-D flaws, coupled with Monte-Carlo simulations to characterize the key fracture toughness parameters in assessments of vessel integrity. The Fracture Analysis of Vessels – Oak Ridge (FAVOR), a computer code developed and maintained by the Oak Ridge National Laboratory (ORNL), provides a convenient tool to calculate mode I, linear-elastic stress-intensity factors ( $K_I$ ) for 3-D, curved flaws in the wall of an RPV. Stress redistribution in the real, elastic-plastic material behavior generally elevates the stress values adjacent to the otherwise linear-elastic, asymptotic crack-tip field, and leads to increases of the crack driving force measured in terms of  $K_I$ . Under elastic-plastic deformations, the interactions between the base (wall) and cladding materials of the RPV (with mismatched yield strengths) impose a potential effect on the crack-front stress fields near the base-cladding interface. The effects of nonlinear material response near the crack front and the interaction between the base and cladding materials under severe thermal-mechanical loading conditions likely require a more accurate numerical description implemented in the framework of elastic-plastic fracture mechanics. The elastic-plastic analyses of RPVs under severe thermal-mechanical transients described here establish benchmark cases for future efforts to approximate the elastic-plastic crack-front region by a simpler,  $K_I$ - $T$  field in a 2-D, small scale yielding (SSY) configuration.

The scalar Weibull stress value can be used to characterize the local conditions for cleavage fracture along the front of an embedded flaw in an RPV. Computation of the Weibull stress integrates (numerically) an “effective” stress over a small fracture process zone surrounding the crack front. The value of the Weibull stress thus depends on the Weibull modulus ( $m$ ), which characterizes the size distribution of microcracks in the material, and the size of the fracture process zone, defined by the stress cutting parameter ( $\lambda$ ). A properly calibrated Weibull exponent,  $m$ , and a suitably defined  $\lambda$  determine directly the Weibull stress value, and thus affect the predicted cumulative probability of failure.

Applications of the Weibull stress framework to RPVs under PTS conditions rely upon extensive previous research efforts [25-28, 39, 40] on the calibration schemes for various Weibull stress parameters of ferritic steels. These earlier works address the effects of crack-front constraint and the temperature dependence (or independence) of the Weibull stress parameters for through-crack fracture specimens with

uniform temperature along the crack front. In contrast, the curved, 3-D crack fronts in the wall of an RPV experience potentially significant temperature gradients, which lead to variations in material properties and thermal loadings along the front. The temperature dependent Weibull scaling parameter,  $\sigma_u$ , and the Weibull threshold stress,  $\sigma_{w-min}$ , thus vary along the crack front. Applications of the 3-D Weibull stress framework to the embedded flaws in RPVs would require enormous numbers of complex 3-D models and nonlinear analyses; therefore, simplifications are needed for realistic engineering applications.

The present study first examines the accuracy of different finite element types and models of material behavior on the computed values of macroscopic crack driving forces ( $K_I$ ) along the front of an embedded flaw in the wall of an RPV under two realistic thermal and mechanical transients. The numerical investigation compares stress-intensity factors computed using the (linear-elastic) FAVOR code with the fully elastic-plastic analyses performed in the finite element code, WARP3D [36]. An independent numerical procedure computes the Weibull stress values from the 3-D stress fields obtained from the detailed, elastic-plastic finite element analyses. Effects of two definitions for the Weibull “effective” stress are examined together with values specified for the stress cutting parameter ( $\lambda$ ). Based on the current investigation and previous research work on the Weibull stress model [28, 39, 40], this study proposes a refined, a simplified and a  $K_I$ - $T$  approximation approach for integrity assessments of RPVs with crack-like defects under pressurized thermal shock events. The refined procedure divides the entire crack front into different subregions with a uniform temperature and a constant  $K_I$ -value within each subregion. The total Weibull stress obtained through this procedure reflects a temperature-dependent  $\sigma_u$ -value along the front. The simplified procedure adopts a uniform material toughness for the entire crack front. The  $K_I$ - $T$  methodology approximates the nonlinear 3-D crack-front fields with an equivalent  $K_I$ - $T$  field on a 2-D SSY configuration.

## **Acknowledgements**

---

This investigation was supported by grants principally from the U.S. Nuclear Regulatory Commission, Office of Regulatory Research and from the Naval Surface Warfare Center, Carderock Division. Additional financial support was provided by the M.T. Geoffrey Yeh Endowed Chair Fund in the Department of Civil & Environmental Engineering at the University of Illinois. We wish to acknowledge the many valuable discussions and data contributions from Dr. Kim Wallin, VTT (Finland), Dr. Mark T. Kirk, Nuclear Regulatory Commission (NRC), and Dr. Charles Roe, Naval Surface Warfare Center (NSWC).

This page is intentionally blank.

## Acronyms

---

DBT = ductile-to-brittle transition

EPFM = elastic-plastic fracture model

FAVOR = fracture analysis of vessels – Oak Ridge

LEFM = linear-elastic fracture model

LSY = large-scale yielding

PTS = pressurized thermal shock

RPV = reactor pressure vessel

SSY = small-scale yielding

C(T) = compact tension specimen

SE(B) = single-edge notched bend specimen

ASME = American Society of Mechanical Engineers

ASTM = American Society for Testing and Materials

ORNL = Oak Ridge National Laboratory

This page is intentionally blank.

# 1 Introduction

---

Reactor pressure vessels (RPVs) are thick-walled, cylindrical steel structures enclosing the reactor core in a nuclear power plant. RPVs experience a wide range of complex, thermal-mechanical loadings during their service life. Pressurized thermal shock (PTS) refers to an accident scenario in an RPV that causes severe cooling concurrent with or followed by significant pressure changes within the vessel. Non-uniform temperature distributions and subsequent differential expansions and contractions generate potentially significant tensile stresses in the vessel and thereby elevate the load intensity on any crack-like defect located in an RPV. Rapid cooling at a high internal pressure may cause conditions that increase the potential for crack initiation and cleavage (brittle) fracture at critical locations in the wall of an RPV. Deterministic fracture mechanics assessments become extraordinarily challenging in view of the complex geometry and transient thermal-mechanical loading histories, coupled with a wide range of potential crack sizes, shapes, and locations in the vessel wall. However, limited studies using deterministic fracture mechanics offer an opportunity to benchmark various simplified, probabilistic fracture mechanics schemes, which provide a more convenient and computationally affordable tool for the failure assessment of RPVs under PTS conditions. Such simplified probabilistic approaches [1-2] adopt principles of linear-elastic fracture mechanics (LEFM) to make the computational effort tractable, even though significant plastic deformation would often occur along the front of a critical crack during a PTS event.

Over the past two decades, significant computational modeling has generated catalogs of linear-elastic solutions for 3-D crack configurations of the type that can develop in RPVs [3-7]. The Oak Ridge National Laboratory (ORNL) in the U.S. leads the work to formulate the extensive database of stress-intensity-factor influence coefficients (*i.e.*, weight functions) for flaws located in the wall of an RPV [6, 7]. The Fracture Analysis of Vessels – Oak Ridge (FAVOR), a computer code developed and maintained by ORNL, incorporates these weight functions to compute linear-elastic, mode I stress-intensity factors for realistic 3-D flaws in RPVs, with accuracy ensured through extensive benchmark studies [8, 9]. Probabilistic assessments of vessel integrity, for example, as performed using the FAVOR code [10, 11], employ various superposition schemes made possible by the assumption of linear-elastic behavior to make tractable Monte Carlo analyses on desktop PCs (statistical sampling of crack size, shape, orientation, position, loading transient, etc.).

Probabilistic assessment of vessel integrity also requires a realistic modeling of the expected statistical variations in fracture toughness of the ferritic steels used to construct RPVs. The probabilistic treatment of cleavage fracture toughness utilizes a statistical description [12] (typically the weakest link model [13-16]) for the transgranular cleavage mechanism in ferritic steels. The Weibull stress framework, originally proposed by the Beremin group [16, 17], assumes that there exist small, but finite, volumes of material which fully embody a population of flaws, whose size and density constitute material properties. The cumulative probability of fracture depends on the statistical distribution of the microcracks, which can be characterized by the so-called Weibull stress using the Griffith fracture criterion [18]. The Weibull stress framework has become a commonly recognized approach to quantify the driving force for cleavage frac-

ture [19-22], to characterize material toughness properties [23, 24], and to develop and apply constraint corrections [25-27] which accommodate differences in crack-front conditions between small laboratory test specimens and RPVs. Recent work by Petti and Dodds [28] suggests that coupling of the Weibull stress approach and the macroscopic Master Curve concept (as outlined in ASTM E-1921 [29]) can dramatically reduce the (laboratory) testing of fracture specimens required for calibration of parameters in the Weibull stress model for a specific ferritic steel. The outcome is a new modeling process that attains the simplicity of an “engineering” approach for assessment of vessel integrity for a cleavage fracture event.

Current research efforts in the U.S. and Europe aim to extend the linear-elastic fracture mechanics (LEFM) framework as represented by FAVOR to include effects of elastic-plastic deformation along the fronts of 3-D flaws to support a more accurate (and realistic) estimation of the probability of cleavage fracture in an RPV. This new work is driven by the following two developments in recent years: the widespread application of the Master Curve approach to characterize the cleavage fracture toughness of RPV steels for elastic-plastic conditions that occur over the ductile-to-brittle transition region [30-32], and developments in the analytical-computational methods that make possible approximate treatments of plasticity on driving forces for complex geometries ( $K_I$  coupled with the  $T$ -stress) [33, 34]. Kirk and Mitchell [35] describe potential applications of the Master Curve concept in characterizing the fracture toughness for PTS assessments of reactor pressure vessels. Recently, thirty-four researchers representing twenty-five organizations from thirteen countries participated in an international project titled "International Comparative Assessment Study of Pressurized Thermal Shock in Reactor Pressure Vessels (RPV PTS ICAS)" [34]. This project performed a comparative evaluation of analysis methodologies employed in the assessment of RPV integrity under PTS conditions. The assessment methodologies reflect the work of three task groups: deterministic fracture mechanics (DFM), probabilistic fracture mechanics (PFM) and thermal-hydraulic mixing (THM). One outcome of this effort is a conflicting set of stress-intensity factor values computed for embedded and surface breaking defects in RPVs that differ based on model refinement, element type and meshing details.

The current study continues and extends these efforts. The macroscopic crack driving force,  $K_I$ , is computed along the crack front for axially and circumferentially embedded flaws in two benchmark PTS transients, denoted here as Transients A and B. The computational models employ very detailed, 3-D finite element meshes built from 8-node or 20-node brick elements, with linear-elastic or elastic-plastic material properties. The computed crack driving force ( $K_I$ ) provides a measure to compare the (current) linear-elastic version of the FAVOR code with the detailed, elastic-plastic analyses which represent more closely the nonlinear response along the crack front. This comparison builds key benchmark solutions for future, planned efforts to approximate the elastic-plastic material behavior near the crack front using a simplified, linear-elastic  $K_I$ - $T$  field coupled with Weibull stress computations for 2-D (plane-strain) small-scale yielding (SSY) models. The current study also computes Weibull stress values along the entire front of the embedded cracks to explore different effective stress definitions and details of the numerical procedure. The existing Weibull stress framework successfully characterizes the probabilistic aspects of cleavage fracture for through-thickness cracks, in laboratory test specimens. In such cases, the

local variations of  $K_I$  and local Weibull stress values along the (relatively) straight crack fronts pose no significant difficulties in applications of the Weibull stress model. For embedded cracks in RPVs, with strong variations of the crack driving force along the curved fronts from through-wall thermal gradients, the proper application of the Weibull stress model becomes considerably more complex. Some preliminary numerical results for Weibull stress values computed for embedded flaws in RPVs under PTS transients are presented to guide future work. To motivate follow-on efforts, the current study proposes refined and simplified Weibull stress approaches for embedded cracks in RPVs under PTS events.

The organization of this report is as follows. Section 2 describes briefly the computational procedure adopted in the FAVOR code and key features of the domain integral approach to incorporate thermal loading as implemented in the WARP3D code. A short summary of the Weibull stress model is included for completeness. Section 3 outlines the finite element modeling procedures employed here, including the geometry of the RPVs, material properties, the transient loading conditions and the details of the constructed models, using 8-node and 20-node brick elements. Section 4 compares the crack driving forces, characterized by linear-elastic  $K_I$ -values and elastic-plastic  $K_I$ -values, computed for Transients A and B. Section 5 provides Weibull stress values for the axially embedded flaw under the Transient A, and explores two definitions of the kernel for the Weibull stress integral and definitions of the fracture process zone. Section 6 outlines the simplified and refined approaches to apply the Weibull stress model in the assessments of RPVs with embedded cracks. Section 7 summarizes the conclusions drawn from this study.

This page is intentionally blank.

## 2 Computational Procedures and the Weibull Stress Model

---

### 2.1 FAVOR Code

The Oak Ridge National Laboratory (ORNL) develops and maintains a computer code, the “Fracture Analysis of Vessels – Oak Ridge” (FAVOR), to perform deterministic and probabilistic fracture mechanics analyses of nuclear reactor pressure vessels subjected to pressurized thermal shock and other pressure-thermal events [10, 11]. FAVOR computes the temperature profile through the wall of an RPV over the time history of an event by solving the transient heat conduction equation for a 1-D axisymmetric finite element model of the combined cladding and base materials in the vessel wall. FAVOR also performs a linear-elastic, finite element, thermal-mechanical stress analysis using a 1-D, axisymmetric model for the vessel wall. The stress values derive from the computed displacements through a linear, strain-displacement relationship and a linear-elastic stress-strain relationship. These stress values approximate the loading of material in a vessel wall (no openings or discontinuities) in the absence of a crack. FAVOR computes values of the linear-elastic stress-intensity factors using the principle of superposition. Flaws are assumed to experience only mode I loading and plastic zones near the crack front are assumed to remain vanishingly small. With these assumptions, FAVOR computes the mode I stress-intensity factors for realistic, three-dimensional geometries containing embedded flaws through a comprehensive library of weight functions (stress-intensity-factor influence coefficients), and for surface flaws with a finite or infinite length. Nominal stresses from the 1-D axisymmetric solutions, that vary over the wall thickness, provide the “applied” stresses to scale and to integrate the weight function values. Prior research using the ABAQUS code (<http://www.simulia.com>) for generation of the weight function values ensures acceptable accuracy of FAVOR  $K_I$  values. The stress-intensity factors computed using FAVOR in the current study refer to the mode I stress-intensity solutions for an embedded crack in the wall of an RPV. The ongoing developments for the FAVOR code include many advanced technologies from the latest research work [10, 11].

### 2.2 Computation of $J$ Integral Values for Mechanical and Thermal Loading

The current study employs the domain integral approach implemented in the finite element research code WARP3D [36] to compute the linear-elastic and elastic-plastic crack driving forces along 3-D curved crack fronts subjected to combined mechanical and thermal loading. The local energy release rate at a point  $s$  along a 3-D, non-growing crack front under static and thermal loadings follows from,

$$J(s) = \lim_{\Gamma \rightarrow 0} \int_{\Gamma} \left[ W n_1 - P_{ji} \frac{\partial u_i}{\partial X_1} n_j \right] d\Gamma, \quad (1)$$

where  $\Gamma$  is a vanishingly small contour in the plane normal to the crack front at  $s$ , and  $n$  is the unit vector normal to the contour  $\Gamma$ .  $W$  is the strain energy density, and  $P_{ji}$  is the component of the nominal stress tensor (1st Piola-Kirchhoff stress tensor), which is the non-symmetric tensor denoting the stress components based on the undeformed geometry.  $X_1 - X_2 - X_3$  form a local Cartesian coordinate system at point

$s$  along the crack front with an origin at the crack-tip.  $X_3$  lies tangent to the crack front at  $s$  in the crack plane, while  $X_1$  and  $X_2$  lie in the plane normal to the crack front at  $s$ , with  $X_2$  perpendicular to the crack plane.

In the domain-integral approach for a three-dimensional crack front, Eq. 1 becomes a surface integral defined over a small tube-shaped region from point  $s_a$  to  $s_c$ ,

$$\overline{J}_{a-c} = \lim_{\Gamma \rightarrow 0} \int_{s_a}^{s_c} [J(s)q(s)] d\Gamma = \overline{J}_1 + \overline{J}_2, \quad (2)$$

where  $s$  denotes a position along the crack front, and  $q(s)$  is a weight function, essentially defining a virtual displacement field in the direction of crack extension. With application of the divergence theorem, the energy release rate under static loading,  $\overline{J}_1$ , and the energy release rate under thermal loading,  $\overline{J}_2$ , become

$$\overline{J}_1 = \int_{V_{orig}} \left( P_{ji} \frac{\partial u_i}{\partial X_1} \frac{\partial q}{\partial X_j} - W \frac{\partial q}{\partial X_1} \right) dV_{orig}, \quad (3)$$

$$\overline{J}_2 = - \int_{V_{orig}} \left( \frac{\partial W}{\partial X_1} - P_{ji} \frac{\partial^2 u_i}{\partial X_j \partial X_1} \right) q dV_{orig}, \quad (4)$$

where  $V_{orig}$  represents the undeformed volume of the finite domain surrounding the crack-tip. The  $\overline{J}_2$  integral vanishes for homogeneous, elastic material (linear or nonlinear) in the absence of thermal strains.

Replacing  $P_{ji}$  by the conventional Cauchy stress tensor,  $\sigma_{ij}$ , for small strains and small displacement gradients, Eq. 4 further simplifies to,

$$\overline{J}_2 = \int_{V_{orig}} \sigma_{ij} \left( a_{ij} \frac{\partial \overline{\Theta}}{\partial X_1} + \overline{\Theta} \frac{\partial a_{ij}}{\partial X_1} \right) q dV_{orig}, \quad (5)$$

where  $\overline{\Theta}$  refers to the deviation of temperature from a reference temperature, and  $a_{ij}$  denotes the tensor of thermal expansion coefficients. For a constant (isotropic) thermal expansion coefficient,  $a$ , Eq. 5 becomes,

$$\overline{J}_2 = \int_{V_{orig}} a \sigma_{ij} \frac{\partial \overline{\Theta}}{\partial X_1} q dV_{orig}. \quad (6)$$

The  $J$ -integral value at point  $s_b$  derives from the mean-value theorem over the interval  $s_a < s < s_c$ .

$$J(s_b) \approx \frac{\int_{s_a}^{s_c} J(s)q(s)ds}{\int_{s_a}^{s_c} q(s)ds} = \frac{\overline{J}}{A_q}. \quad (7)$$

The crack driving force, denoted as an equivalent stress-intensity factor,  $K_J$ , follows from the  $J$  integral value,

$$K_J = \sqrt{\frac{JE}{1-\nu^2}}, \quad (8)$$

for the assumption of effectively plane-strain conditions locally along the front of an embedded crack in the vessel wall. The conversion to an “equivalent”  $K_J$ -value applies strictly under linear-elastic and small-scale yielding conditions (as implied in ASTM E-1921). Consequently,  $K_J$ -values computed here using WARP3D for linear-elastic material response are directly comparable to  $K_I$ -values computed using FAVOR for the same configuration and loading. Under elastic-plastic conditions,  $K_J$ -values typically exceed  $K_I$ -values due to load redistribution of plastically deforming material along the crack front. The  $J \rightarrow K_J$  conversion thus provides only a “convenient” value for comparison to  $K_I$ -values computed for linear-elastic material response.

### 2.3 Weibull Stress Model

The weakest link model assumes that fracture of an entire volume of material depends on a single initiator [12, 37, 38], or equivalently a single microcrack. Weakest link concepts form the technical basis for the first testing standard developed specifically to address the unique statistical issues with ferritic steels at temperatures over the ductile-to-brittle transition region (ASTM E1921 [29]). The *macroscopic* fracture model, as outlined in ASTM E-1921, assumes that the temperature, the local stress field and the local  $J$ -values remain essentially uniform along the entire crack front and that small-scale yielding conditions prevail at the cleavage fracture event. SSY conditions insure the unique correspondence across specimens between the crack-front  $J$ -value and the local crack-front strains-stresses at fracture. The corresponding *microscopic* fracture model employs directly the strains-stresses at each crack-front location. SSY conditions then become unnecessary to establish the link with the scalar measure ( $J$ ) of the loading. The Beremin group [16] introduced the most widely used microscopic model. In this model, a local fracture parameter, the so-called Weibull stress ( $\sigma_w$ ), defines an integrated, scalar measure of the crack-front conditions driving cleavage fracture at increasing levels of external loading. Numerical analyses connect values of  $\sigma_w$  with external loading of the specimen-structure and may include complexities from variable crack-front geometry, cladding, large-scale yielding, thermal-mechanical loading, etc.

By correlating an assumed, inverse-power density distribution of critical microcrack sizes with the local stress through a simple fracture mechanics model, the Beremin group [16] derived the cumulative failure probability for a two-parameter Weibull stress model,

$$P_f(\sigma_w) = 1 - \exp\left[-\left(\frac{\sigma_w}{\sigma_u}\right)^m\right], \quad (9)$$

where  $m$  is the Weibull modulus, the value of which depends on the statistical distribution of microcrack sizes in the material, and the scalar Weibull stress,  $\sigma_w$ , follows,

$$\sigma_w = \left[ \frac{1}{V_0} \int_{V_f} \sigma_{eff}^m dV_f \right]^{1/m}. \quad (10)$$

The Weibull scale parameter,  $\sigma_u$ , denotes the Weibull stress value at a cumulative fracture probability of 0.632, or  $P_f(\sigma_w = \sigma_u) = 0.632$ .  $V_0$  defines the (normalizing) reference volume and  $V_f$  represents the fracture process zone. The practical approach to compute the Weibull stress employs numerical integration of an “effective” stress measure,  $\sigma_{eff}$ , over the fracture process zone at each loading level imposed on the finite element model. The effective stress most often takes the value of the maximum principal stress,  $\sigma_1$ , or the hydrostatic stress,  $\sigma_H = (\sigma_1 + \sigma_2 + \sigma_3)/3$ .

The fracture process zone contains a region of plastically deformed, crack-front material over which the effective stress exceeds a characteristic value,  $\lambda\sigma_0$ , with a typical value of  $\lambda = 2$  (here  $\sigma_0$  denotes the uniaxial, tensile yield stress). The normalizing volume,  $V_0$ , cancels in applications of the Weibull stress model to compare crack-front conditions for the same material and takes a value of unity in this paper. The numerical implementation of the Weibull stress calculation follows,

$$\sigma_w = \left[ \frac{1}{V_0} \sum_{n_e} \int_{-1}^1 \int_{-1}^1 \int_{-1}^1 \sigma_{eff}^m |J_{Jac}| d\eta_1 d\eta_2 d\eta_3 \right]^{1/m}, \quad (11)$$

where  $n_e$  denotes the number of elements inside the fracture process zone, and  $|J_{Jac}|$  defines the determinant of Jacobian between the global coordinate system  $(x, y, z)$  and the element local coordinate system  $(\eta_1, \eta_2, \eta_3)$ .

Petti and Dodds [28] propose a Weibull stress-based, three-parameter cumulative probability of fracture model, which requires a minimum threshold Weibull stress to obtain non-zero probabilities of fracture, as given in Eq. 12,

$$P_f(\sigma_w) = 1 - \exp \left[ - \left( \frac{\sigma_w^{m/4} - \sigma_{w-min}^{m/4}}{\sigma_u^{m/4} - \sigma_{w-min}^{m/4}} \right)^4 \right]. \quad (12)$$

The minimum (threshold) Weibull stress,  $\sigma_{w-min}$  [ $\sigma_{w-min} = \sigma_w(K_J = K_{min})$ ], depends on the crack-front length, material flow properties, temperature and Weibull parameters ( $m, V_0$ ) [28]. Equation 12 maintains consistency with the macroscopic, three-parameter expression employed in E-1921 [29] to characterize the cumulative fracture probability, with  $K_J$  as the crack front driving force. For a fixed exponent ( $m$ ), Petti and Dodds [39] demonstrate that the Weibull scaling parameter,  $\sigma_u$ , increases with increasing temperature, which reflects the increasing microscale toughness of ferritic steels caused by local events that include plastic shielding of microcracks, microcrack blunting and microcrack arrest. Further,  $\sigma_{w-min}$  will vary with temperature as the material flow properties vary with temperature over the DBT (even though the macroscopic threshold toughness,  $K_{min}$ , is often assigned a temperature invariant value).

Applications of the Weibull stress model to fracture assessments of RPVs require calibration of the Weibull parameters,  $m, \sigma_u$  and  $\sigma_{w-min}$  (or  $K_{min}$ ). Gao *et al.* [21] developed a new approach to calibrate the Weibull stress parameters ( $m, \sigma_u$ ) for ferritic steels. Their approach derives from the imposed requirement that, over the DBT region, the Weibull stress fracture model predict the macroscopic (1) variation of fracture toughness vs. temperature and (2) statistical variability of toughness values at each tem-

perature over the DBT region as represented by the Master Curve model-procedures reflected in ASTM E1-1921. The calibration procedure employs measured fracture toughness values obtained for high constraint (SSY) and low constraint [large scale yielding (LSY)] configurations. Petti and Dodds [39] utilize the Master Curve characterization of the macroscopic toughness ( $K_{Jc}$ ) vs. temperature relation obtained by as few as six fracture specimens at one temperature to calibrate the Weibull scale parameter,  $\sigma_u$ , as a function of temperature. They demonstrate, through measured properties of two pressure vessel steels (A533B and A508), that the scale parameter,  $\sigma_u$ , increases significantly with temperature for a fixed Weibull modulus,  $m$ , in a three-parameter Weibull stress model. Wasiluk *et al.* [40] present a calibration study of the three parameter Weibull stress model for a 22Ni-MoCr37 pressure vessel steel, utilizing the large-scale datasets from a European Union research project – “Fracture toughness of steel in the ductile to brittle transition regime” [41, 42]. Wasiluk *et al.* [40] demonstrate an effective, temperature invariance of the Weibull modulus,  $m$ , and a temperature dependence of the Weibull scale parameter,  $\sigma_u$ , through calibrations at two extreme temperatures of the ductile-to-brittle transition (DBT) regime for this common RPV steel. The calibration outcome for this type of steel implies that  $K_{min}$  increases gradually with temperature, in contrast to the simpler assumption of a fixed value of  $K_{min} = 20 \text{ MPa}\sqrt{\text{m}}$  adopted in E-1921. Section 5.2 provides additional details on the calibration process to set the Weibull stress parameters for specific materials.

This page is intentionally blank.

## 3 Finite Element Modeling

---

### 3.1 RPV with Embedded Flaws

The current study investigates a reactor pressure vessel containing embedded flaws for two different PTS transients, A and B. Figure 1 illustrates the geometric configuration of the reactor pressure vessel. The designated RPV has an internal radius of  $R_i = 1994$  mm, with a wall thickness of  $t_{wall} = 204$  mm. The height of the cylindrical part in the RPV is 6960 mm. The numerical analyses consider planar elliptical flaws, axial and circumferential, with both embedded near the interface of the base and cladding material. The plane of the circumferentially embedded flaw lies perpendicular to the longitudinal axis of the cylindrical part in the RPV. The plane of the axially embedded flaw lies on the plane formed by the longitudinal axis and the radial axis of the cylinder. Table 1 lists the location parameter ( $d$ ) and dimensions of the embedded cracks. Previous investigations [43] assess the conditional probability of initiation (CPI) and indicate that the selected flaw sizes and locations for study here contribute significantly to the CPI. The circumferential flaw represents an idealized elliptical crack with  $c/a = 10$  and  $2a = 4$  mm, while the axial flaw has an assigned value of  $c/a = 6$ , with  $2a = 17$  mm. The distance  $d$  between the inner edge of the RPV and the nearest point along the crack front is 1.9 mm for the axially embedded flaw and 2.5 mm for the circumferentially embedded flaw. The thickness of the cladding material,  $t_{clad}$ , equals 4 mm for both models.

### 3.2 Material Properties of the Base and Cladding Steels

The base material of the RPV for the models is representative of an ASTM-A533B ferritic steel, with a typical yield strength,  $\sigma_y = 499$  MPa, and the Young's modulus,  $E = 193$  GPa. The cladding material has properties of an austenitic stainless steel with  $\sigma_y = 163$  MPa, and  $E = 157$  GPa. The Poisson ratio is fixed at 0.3 for both materials. Figure 2 shows the uniaxial true stress – logarithmic strain relationship for the ferritic steel and the austenitic steel. The maximum logarithmic strain value equals 2 for the base material to enhance the accuracy of the stress-strain solutions near the crack-front. Beyond the maximum strain specified in Fig. 2, the material properties follow a perfectly plastic response. The coefficient of thermal expansion (CTE) has a value of  $14 \times 10^{-6}$   $1/^\circ\text{C}$  and  $17 \times 10^{-6}$   $1/^\circ\text{C}$  for the base and cladding steels, respectively. With this yield strength and CTE, the cladding steel experiences larger thermal changes in strain and more plastic deformation than does the base steel under a pressurized thermal shock condition. This preliminary study adopts temperature independent properties for both materials (the values above remain constant with variations in the temperature during the transient loading imposed on the computational model).

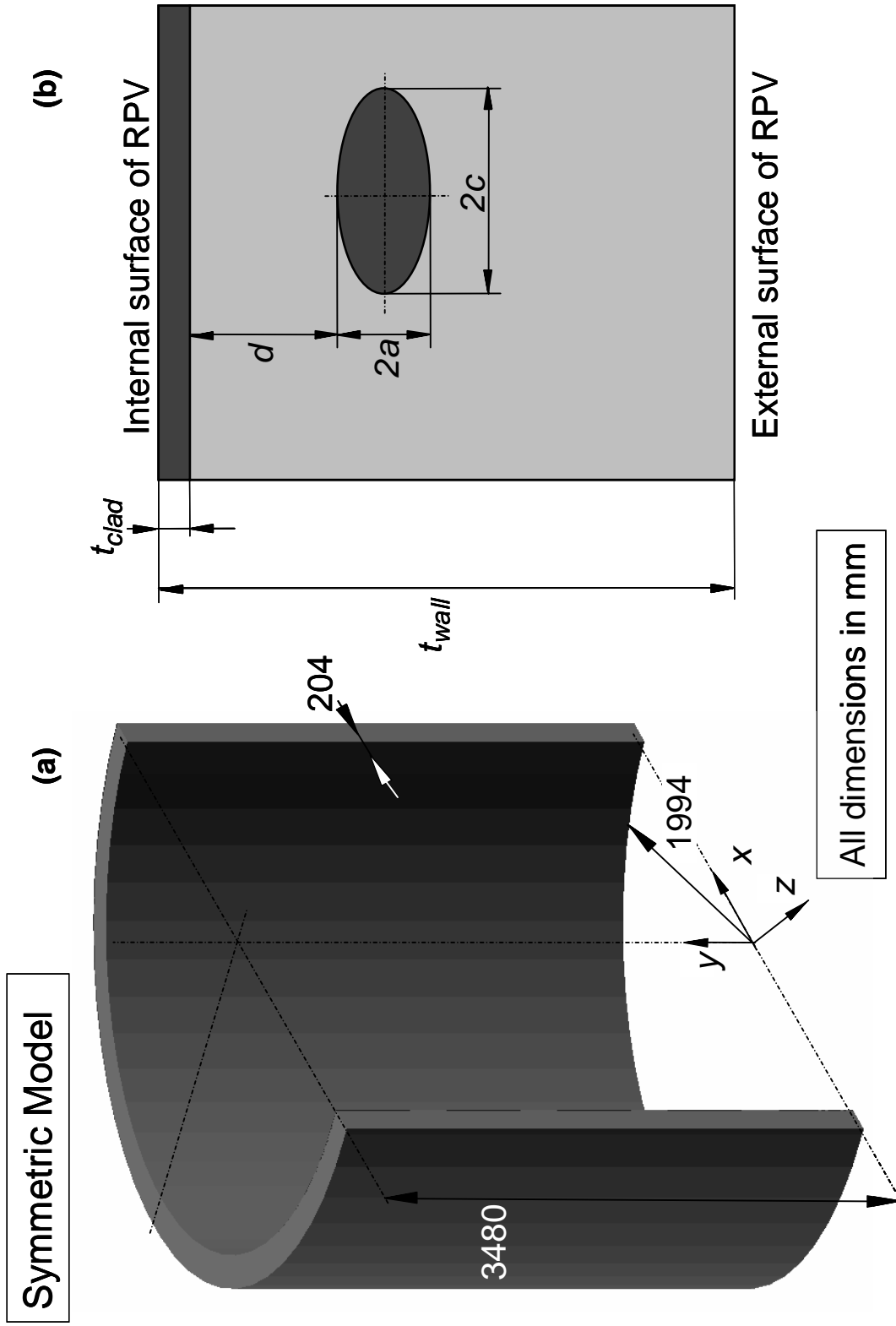


Fig. 1. Geometric configuration of: (a) a quarter symmetric model of a reactor pressure vessel; and (b) an embedded flaw in the wall of the RPV.

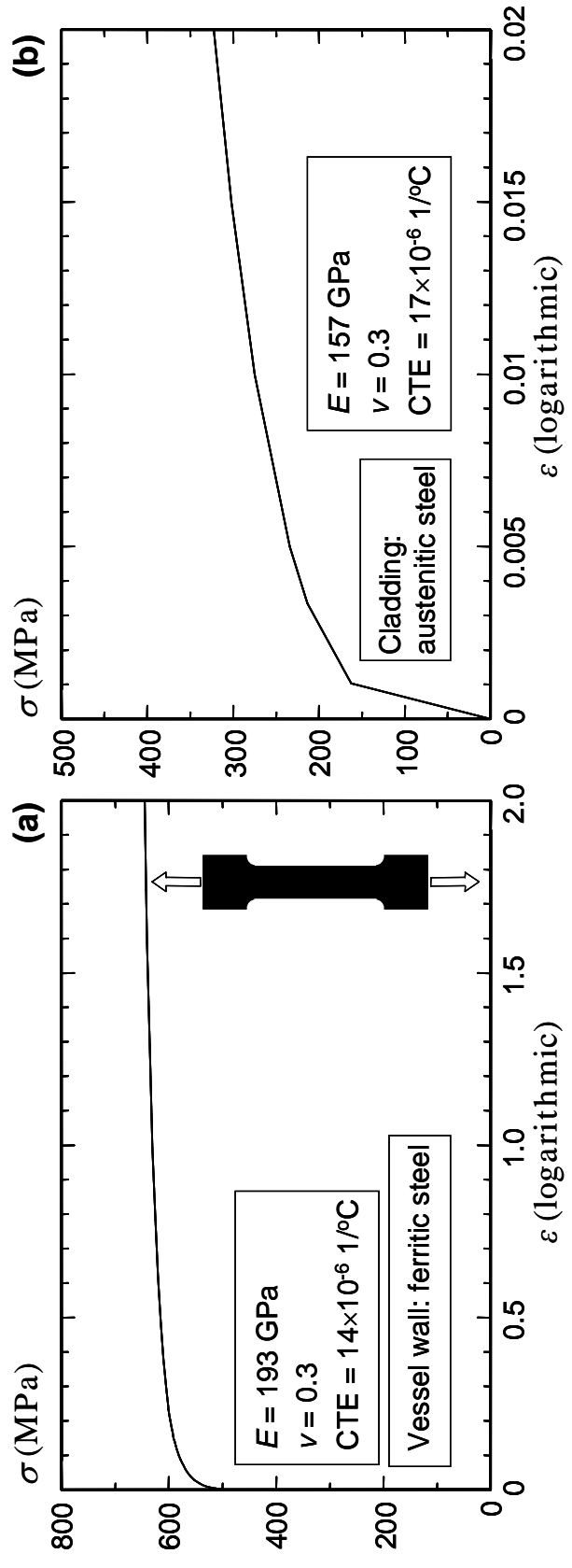


Fig. 2. Uniaxial, true stress-logarithmic strain relationships for: (a) the vessel wall (ferritic) steel of the RPV; and (b) the austenitic stainless steel for the cladding.

**Table 1.** RPV and embedded elliptical flaw dimensions.

<i>Parameters</i> [mm]	<i>Circumferential</i>	<i>Axial</i>
$d$	2.5	1.9
$2a$	4	17
$2c$	41	102
$t_{wall}$	204	
$t_{clad}$	4	
$R_i$	1,994	

### 3.3 PTS Transients

These RPVs with embedded flaws would experience both rapid cooling and internal pressurization changes during a PTS event. Figure 3 illustrates the variations of coolant temperatures and internal pressures for Transients A and B respectively. These transients follow from a risk assessment performed by the Sandia National Laboratories to identify sequences that may be important for risk due to PTS. Variations of the thermal-mechanical responses over the time history for the critical transients are generated using the RELAP5 code [44]. Simple linear interpolation of these cooling temperatures and the internal pressures yields the smoothed thermal and mechanical loading histories for application in the fracture mechanics models. For Transient A, the coolant temperature decreases from 286 °C at  $t=0$  to 43 °C at  $t=18$  min. The internal pressure decreases from 15.9 MPa at  $t=0$  to 0.4 MPa at  $t=20$  min, and then remains at a constant value of 1 MPa for  $t > 21$  min. For Transient B, the coolant temperature decreases from 278 °C at  $t=0$  to 61 °C at  $t=141$  min, and thereafter increases again to 113 °C at  $t=200$  min. As observed on these figures, Transient B shows a more complex mechanical loading history. The internal pressure decreases from 14.5 MPa at  $t=0$  to 6 MPa at  $t=8$  min. The pressure remains approximately at the same value until  $t=139$  min, when the internal pressure increases rapidly to 16.9 MPa at time  $t=147$  min and maintains that level until  $t=200$  min.

With these estimated coolant temperature histories for the PTS event, the FAVOR loading module [10, 11] computes the temperature variation across the wall thickness of the RPV over the time history using deterministic analyses with 1-D axisymmetric models. Figure 4 shows the computed temperature profiles over the normalized wall thickness,  $t_{nom} = (R - R_i) / t_{wall}$ , for Transients A and B at time intervals of 5 minutes, where  $t_{nom} = 0$  indicates the inner surface of the vessel. For Transient A, the temperature near the inner surface decreases rapidly as a result of sudden cooling, which generates high temperature gradients and local bending stresses across the wall thickness. Figure 4b indicates a less severe temperature gradient over the wall thickness for Transient B.

### 3.4 Finite Element Models

The current study employs two types of finite element models constructed using 8-node brick elements and 20-node brick elements, respectively. Both elements are of the isoparametric formulation. A very convenient, MS-Windows-based crack mesh generator, FEACrack [45], is used to build the crack-front mesh, with subsequent, additional mesh generation completed in MSC Patran. For the linear-elastic analyses, the crack-front mesh utilizes collapsed elements sharing a single node at each crack front location. For meshes generated with 20-node elements, the mid-side of the first ring of elements incident on the crack front are positioned at the quarter-point location along the corresponding element edges. For elastic-plastic analyses, elements at the crack front are also collapsed at the same location, but with unique nodes and numbering. The mid-side nodes for the nonlinear models remain at the mid-point location of the element edges for meshes using 20-node elements. For both the linear-elastic and elastic-plastic analyses, the cladding steel at the inner surface of the RPV is modeled with four layers of elements.

Figure 5 shows the 8-node finite element mesh for the RPV with a circumferentially embedded flaw. The presence of two global planes of symmetry permits the use of a quarter-symmetric model. The linear-elastic analysis employs a model with 83,976 elements and 90,500 nodes, while the elastic-plastic analysis utilizes the same number of elements with 90,748 nodes. The finite element model has 30 elements along the full length of the semi-elliptical crack front, with 20 focused domains (rings) of elements for computation of  $J$ -integral values around each crack-front node. Each “domain” then contains 8 elements enclosing each crack-front location, *i.e.*, the mesh resolution in the  $\theta$  direction is 8 elements.

Figure 6 shows the 8-node finite element mesh generated for an RPV containing an axially embedded flaw. The model for the linear-elastic analysis consists of 82,586 elements and 90,176 nodes, and 58,636 elements and 64,587 nodes for the elastic-plastic analysis. The crack front contains a highly refined mesh with 73 elements along the full length of the semi-elliptical crack front.

We investigated the different element types to explore the potential effects on computed  $J$ -values for these thermal loadings with locally severe, spatial gradients. These temperature gradients induce bending-type deformations which cause shear locking behavior in the 8-node brick elements, and thus an overly stiff response. The pressure loading alone generates very smooth, through-wall stress gradients readily accommodated with the fine mesh of 8-node brick elements. The 20-node elements with reduced ( $2 \times 2 \times 2$ ) integration alleviate the shear locking phenomena but are more computationally demanding in these large, refined models. Figures 7 and 8 illustrate the details of the 20-node meshes for RPVs with a circumferentially and an axially embedded flaw, respectively. The crack front contains 30 elements with 20 domains of focused elements to compute the values of the  $J$ -integrals at each crack-front node location.

The 8-node and 20-node meshes share identical, remote boundary conditions. On the two planes of symmetry ( $y = 0$  and  $z = 0$ ), the numerical analysis constrains the displacements perpendicular to the corre-

sponding plane. To avoid remaining rigid body motions, the analysis prevents displacement in the  $x$ -direction for the node located at  $x = 1994$  mm,  $y = 0$  and  $z = 0$ .

To represent the mechanical loading during the PTS event, the analyses apply a spatially uniform pressure on the inner face and a spatially uniform traction on the plane normal to the  $y$ -axis at the remote end ( $y = 3480$  mm) of the model. For these flaws located completely within the wall of the vessel, there is no applied crack face pressure. For the thermal loading, a special software code was developed to assign temperatures to every node of the finite element model over the entire time history with  $\Delta t = 1$  min. The temperature profile over the wall thickness follows the deterministic analyses performed for Transients A and B in FAVOR shown in Figs. 4a and 4b. Simple linear interpolation defines the temperature values for nodes located between positions in the wall thickness included in the FAVOR 1-D model.

Finite element analyses of the 3-D models described above are performed using the research code WARP3D [36] on a high-end (Itanium) HP UNIX workstation. Nonlinear material response follows the Mises constitutive model with  $J_2$  flow theory. The element response follows the finite-strain formulation. The  $\bar{B}$  modification prevents the volumetric locking for 8-node elements during incompressible plastic deformation (but does not improve the shear locking behavior). The  $\bar{B}$  approach makes the 8-node element have constant mean stress over the element volume (this is the only formulation available for the 8-node element in the widely used ABAQUS program, for example). The WARP3D includes domain integral procedures that automatically compute  $J$  values in the specified domains along the crack front.

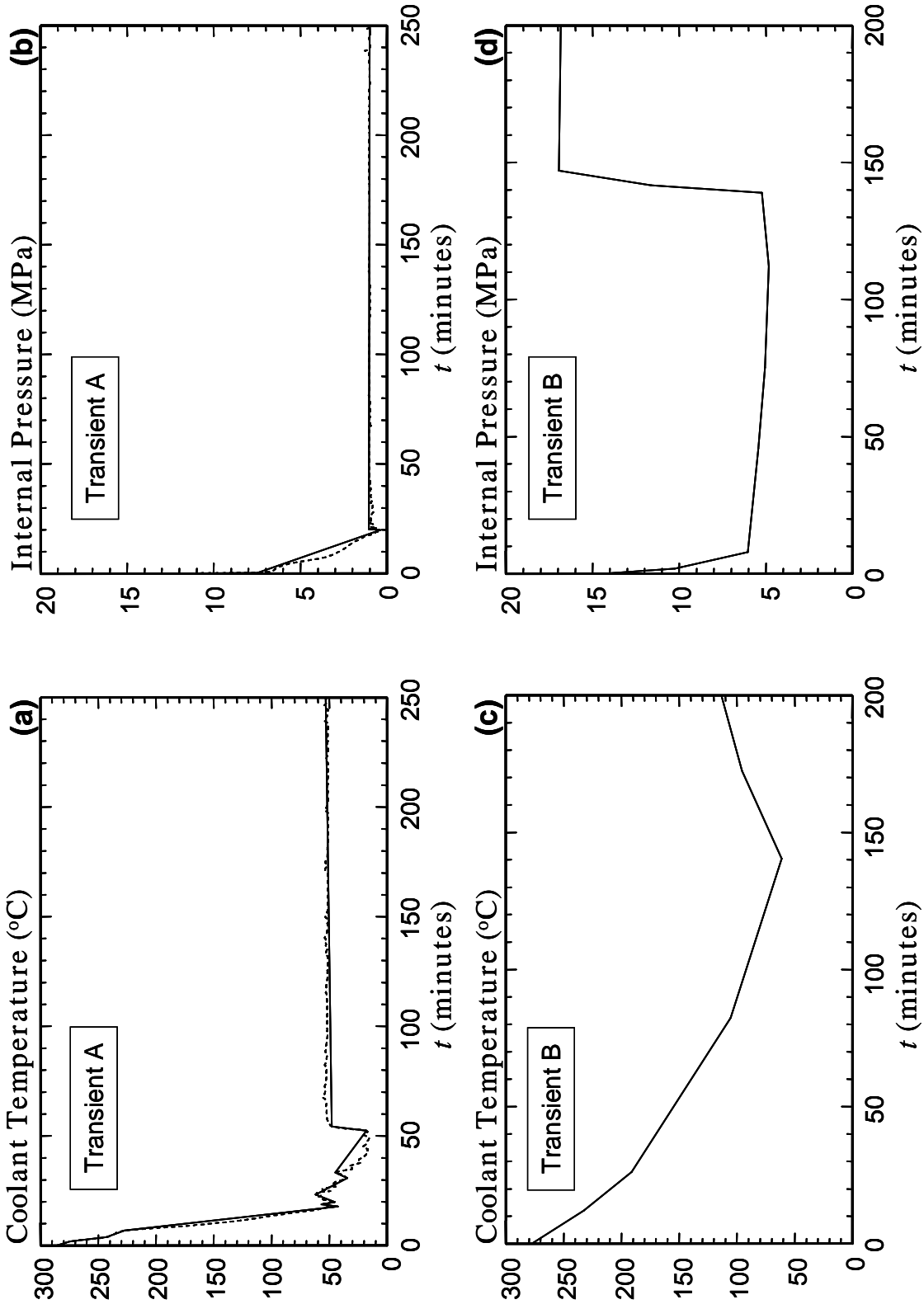


Fig. 3. Transient conditions: (a) Transient A coolant temperature; (b) Transient A internal pressure; (c) Transient B coolant temperature; and (d) Transient B internal pressure. Simple linear interpolations smooth these loading histories for input to the fracture analyses.

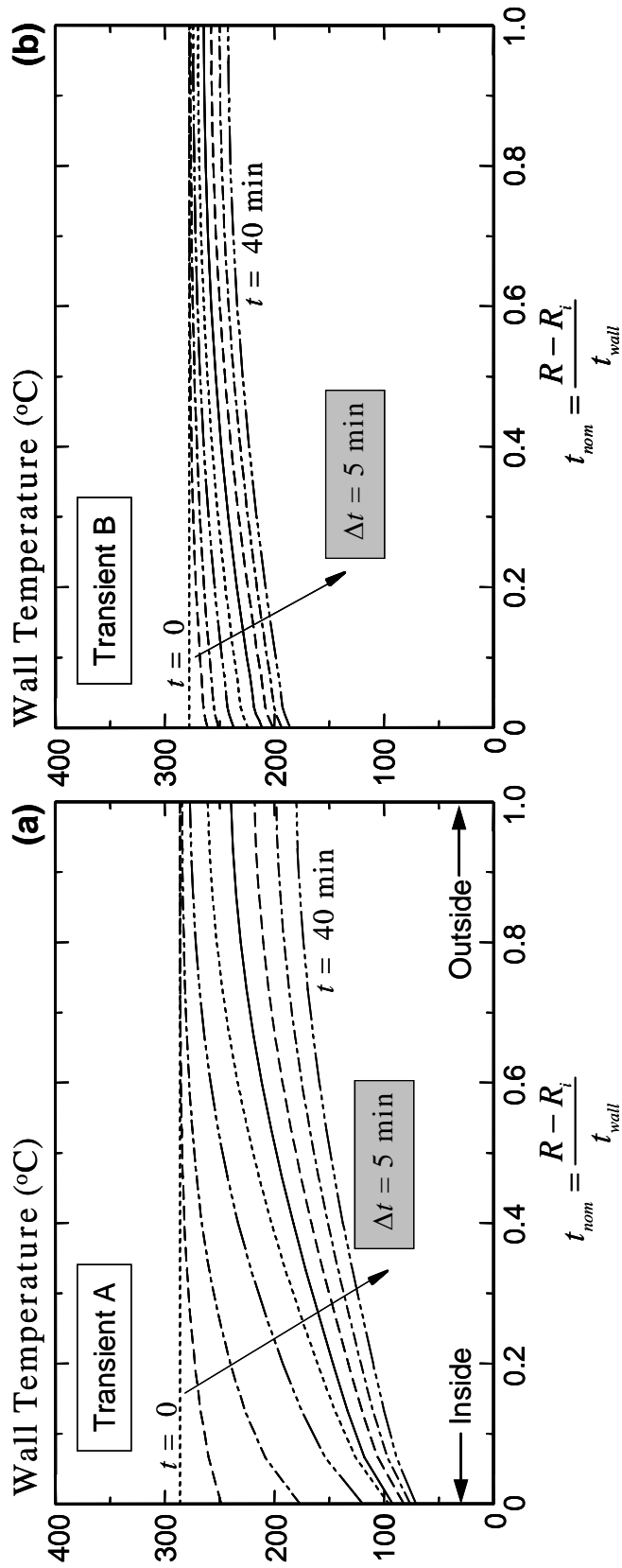


Fig. 4. Temperature variations over the wall thickness at time intervals of 5 minutes computed by the 1-D axisymmetric analysis in FAVOR for: (a) Transient A; and (b) Transient B.

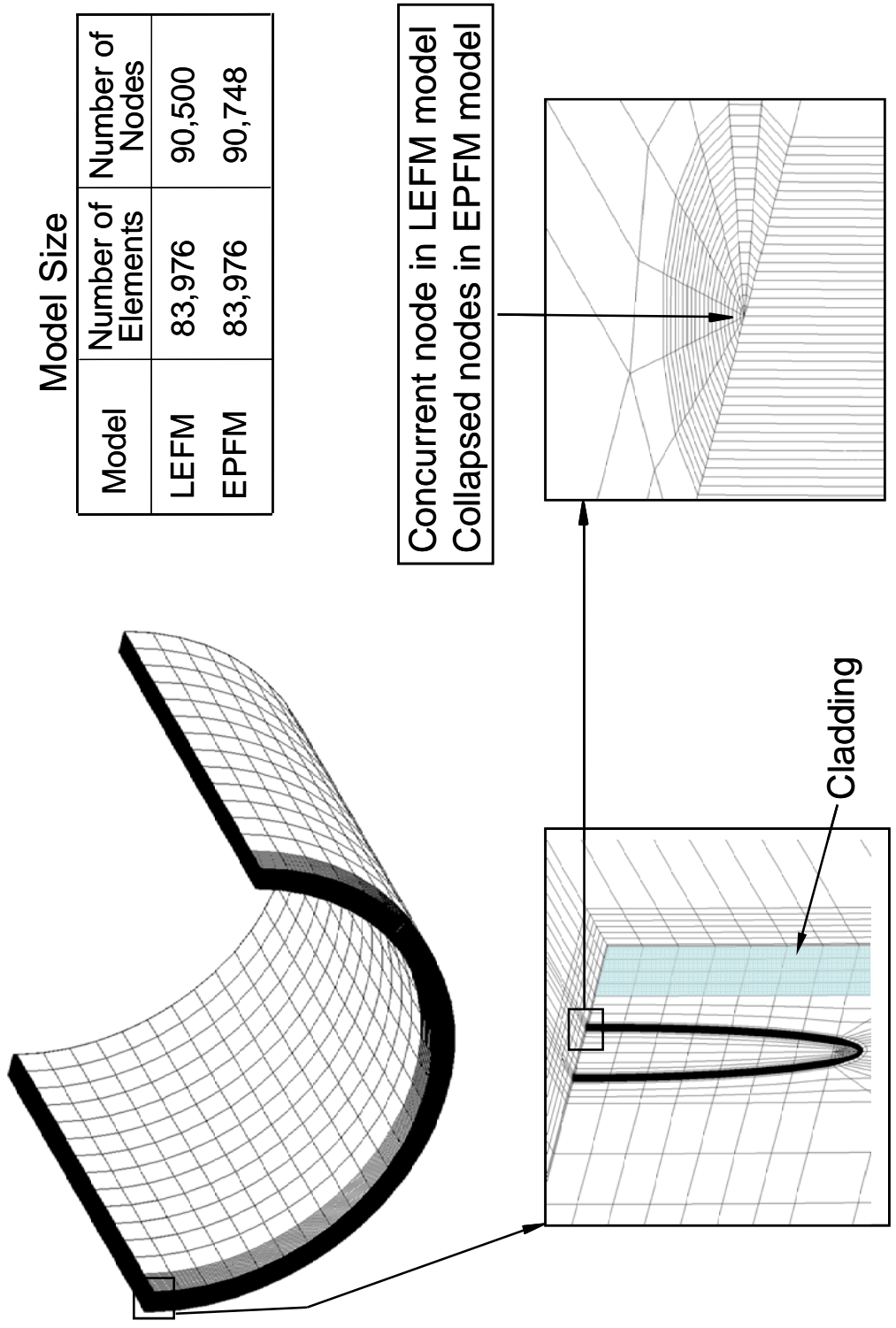


Fig. 5. Models using 8-node brick elements for RPV with a circumferentially embedded elliptical flaw (LEFM = Linear-Elastic Fracture Model; EPFM = Elastic-Plastic Fracture Model).

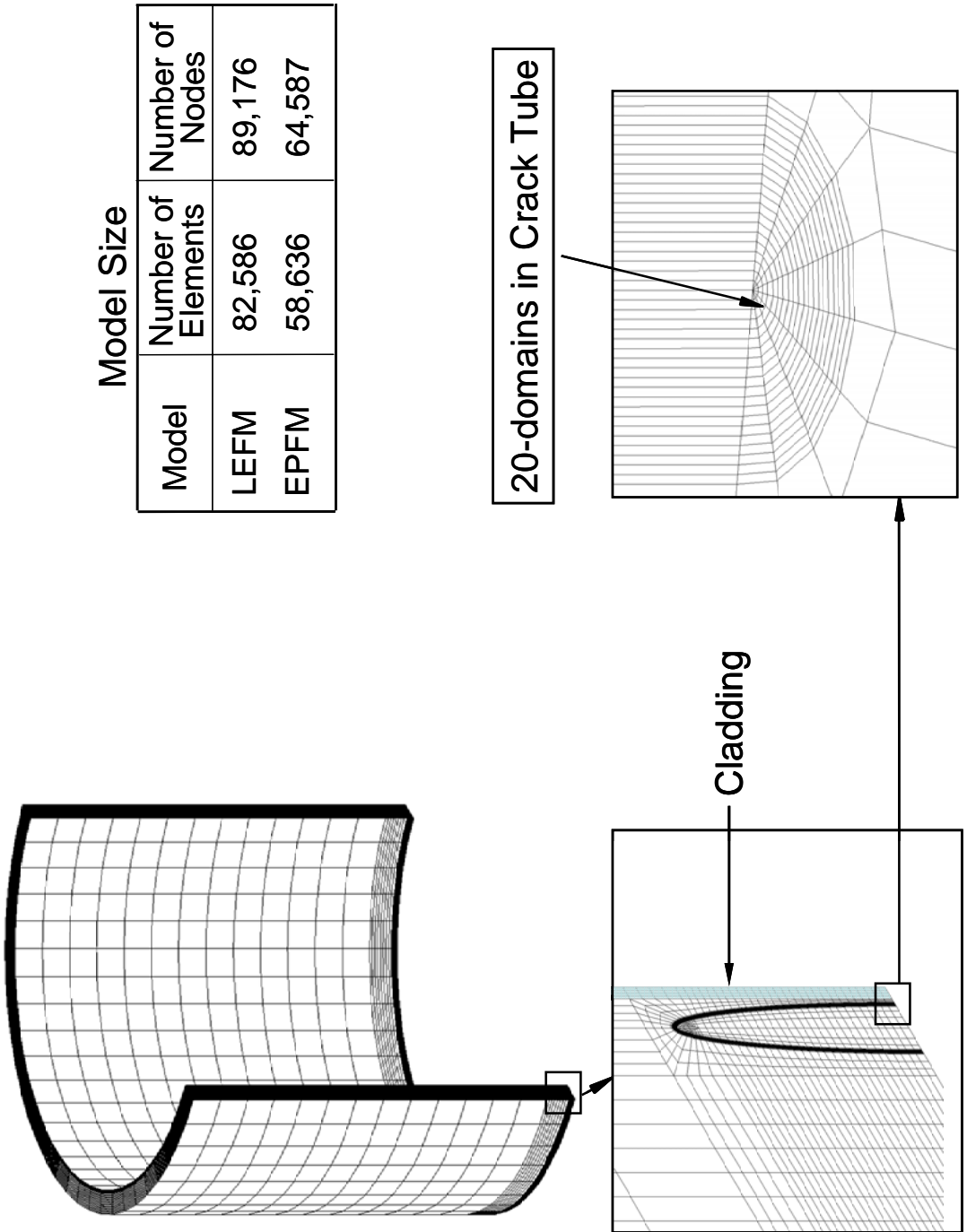


Fig. 6. Models using 8-node brick elements for RPV with an axially embedded elliptical flaw (LEFM = Linear-Elastic Fracture Model; EPFM = Elastic-Plastic Fracture Model).

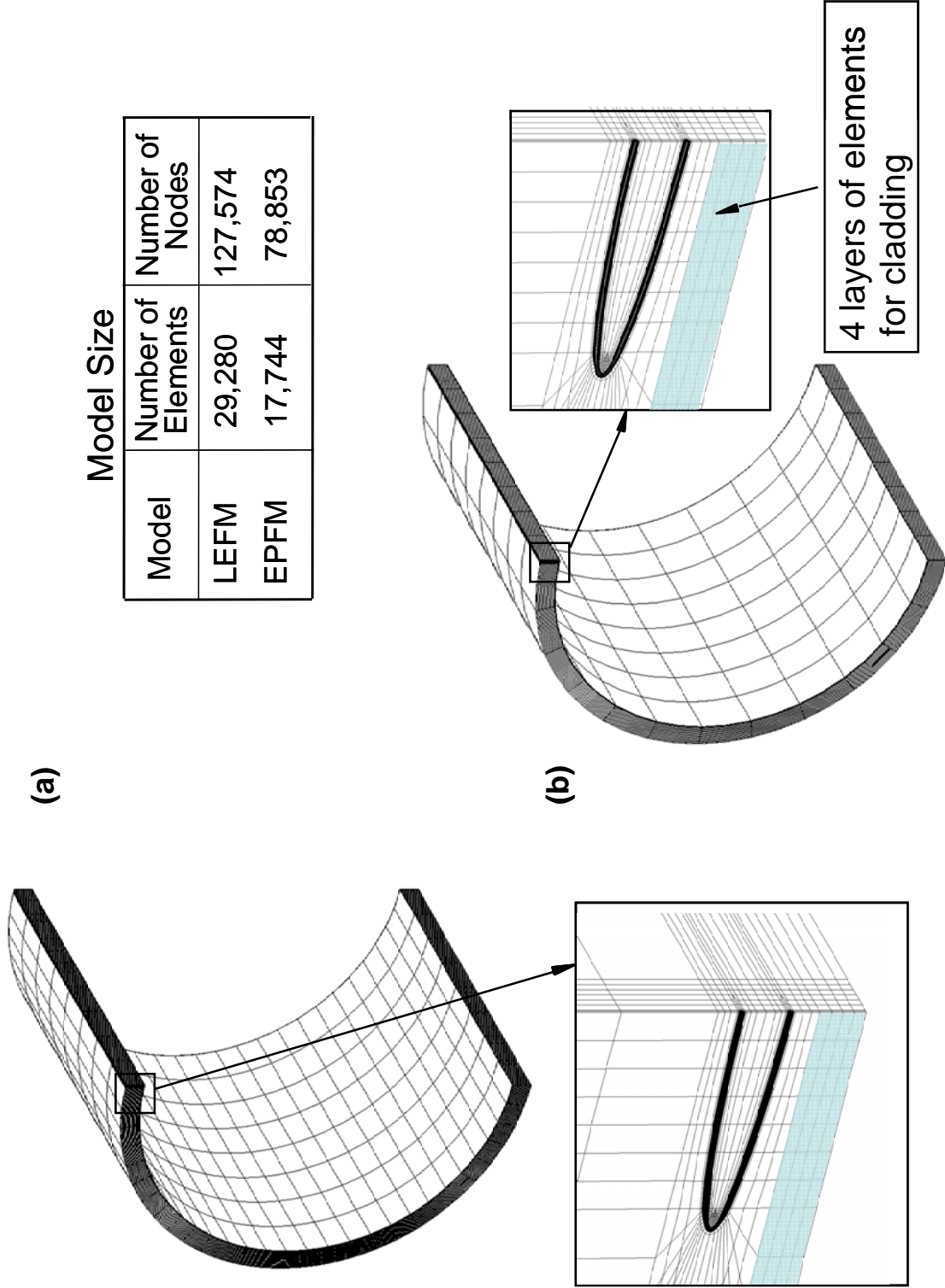


Fig. 7. Models using 20-node brick elements for RPV with a circumferentially embedded elliptical flaw: (a) for linear-elastic analysis; and (b) for elastic-plastic analysis (LEFM = Linear-Elastic Fracture Model; EPFM = Elastic-Plastic Fracture model).

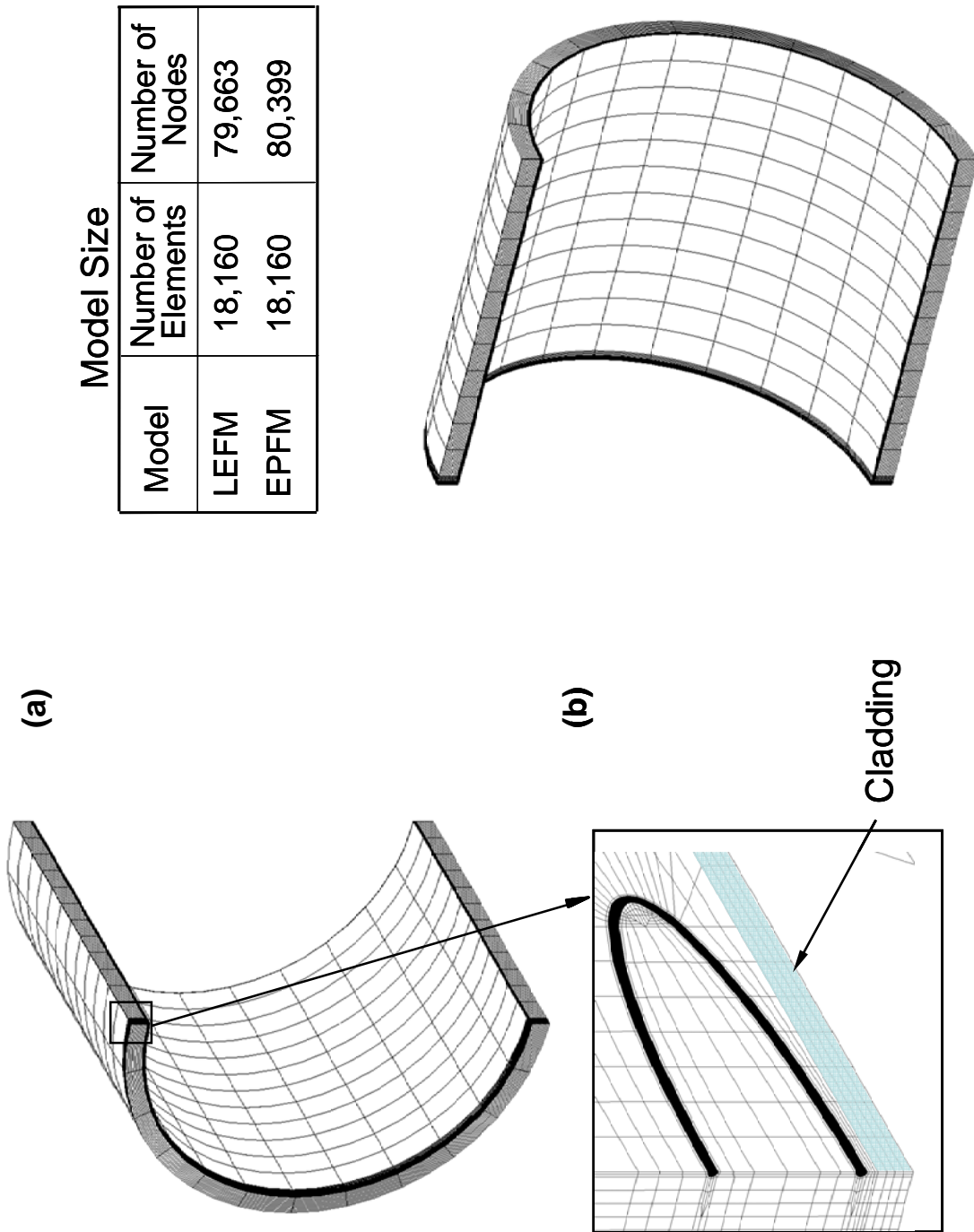


Fig. 8. Models using 20-node brick elements for an RPV with an axially embedded elliptical flaw: (a) for linear-elastic analysis; and (b) for elastic-plastic analysis (LEFM = Linear-Elastic Fracture Model; EPFM = Elastic-Plastic Fracture Model).

## 4 Crack Driving Forces for Two Transients

---

### 4.1 Transient A

Figure 9 shows the linear-elastic, crack driving force,  $K_I$ , along the elliptical crack front computed for both the axially embedded flaw and the circumferentially embedded flaw. The curves show the distribution of  $K_I$  values at three times,  $t = 10$  min, 18 min and 30 min. These results are obtained with 8-node element meshes using the WARP3D code. The linear-elastic  $K_I$ -values are computed from  $J$ -values using the plane-strain conversion,  $K_I = \sqrt{EJ/(1-\nu^2)}$ . The sketch in Fig. 9 illustrates the positive and negative values for the positional angle along the crack front,  $\phi$ . The crack driving force shows a minimum value at  $\phi = 0$  (point A), and increases at locations nearer the inner surface or the outer surface of the RPV.  $K_I$  reaches the maximum value at  $\phi = \pi/2$  (point B), which also experiences the lowest temperature among all the crack-front nodes. Because the maximum crack driving force occurs at  $\phi = \pi/2$ , the stress-intensity factors reported in subsequent figures all refer to  $K_I$  values at  $\phi = \pi/2$ .

Figures 10a and 10b compare the  $K_J$ -values computed using the FAVOR code with the linear-elastic and elastic-plastic values obtained using the 8-node FE models in WARP3D. The values from FAVOR refer to the linear-elastic, mode I stress-intensity factor ( $K_J = K_I$ ), computed from weight functions of SIFs with crack face loadings from the axisymmetric finite element models. The stress-intensity factors from 3-D FE analyses in WARP3D, which include potentially mixed-mode crack driving forces caused by the thermal loading, follow from the  $J$ -integral values using the plane-strain conversion in Eq. 8.  $K_J$ -values from WARP3D are identical to  $K_I$ -values for linear-elastic analyses.

The numerical solution for Transient A terminates at  $t = 50$  min, beyond which the thermal and mechanical loading does not produce a more critical crack-front condition than the loading conditions for  $t < 50$  min (as illustrated in Fig. 3). For the circumferentially embedded crack, peak crack-front loads occur at  $t = 18$  min for all three solutions as illustrated in Fig. 10a. Among the three analyses shown in Fig. 10a, FAVOR predicts the highest  $K_J$ -values. The  $K_J$ -values computed for the (WARP3D) linear-elastic analysis and the elastic-plastic analysis remain approximately equal up to  $t = 14$  min, beyond which the temperature gradient across the wall thickness becomes more significant, causing higher stress-intensity factors in the elastic-plastic solution. At  $t = 18$  min, the linear-elastic solution from WARP3D indicates a 20% lower value than the prediction by the FAVOR code, or  $K_I(\text{FAVOR}) - K_I(\text{WARP3D}) = 7.6 \text{ MPa}\sqrt{\text{m}}$ . The  $K_J$ -value at  $t = 18$  min computed from the elastic-plastic analyses remains 9% lower than the (LEFM) FAVOR solution.

Figure 10b compares the  $K_J$ -values for an elliptical crack (axially embedded) in the wall subjected to Transient A, computed through the FAVOR code and WARP3D analyses (using models with 8-node elements). As found for the circumferentially embedded crack, the stress-intensity factor reaches a peak value again at  $t = 18$  min for all three solutions. The circumferential hoop stress in the wall of a cylindrical vessel (caused by the internal pressure), acting normal to the face of the axially embedded crack, has a value approximately twice as large as the longitudinal axial stress acting perpendicular to the face of a

circumferential flow. The initial internal pressure, therefore, generates more significant plastic deformation near the tip of the axially embedded crack compared to the front region of the circumferentially embedded crack. The stress-intensity factor computed using the elastic-plastic analysis deviates from the linear-elastic solution at an earlier time ( $t \approx 10$  min) for the axially embedded crack, compared to the circumferentially embedded crack which experiences similar magnitudes of linear-elastic and elastic-plastic crack driving force,  $K_I$ , until  $t = 14$  min, as shown in Fig. 10a. At  $t = 18$  min, the linear-elastic stress-intensity factor from WARP3D is 19% lower than the crack driving force predicted using the FAVOR code, while the elastic-plastic stress-intensity factor computed from WARP3D is 7% lower than the FAVOR solution.

The stress-intensity factors computed using the 20-node element models demonstrate significantly higher values compared to the  $K_I$  solutions obtained from the 8-node element models, as illustrated in Figs. 10c and 10d for both linear-elastic and elastic-plastic analyses. For the circumferentially embedded crack, the peak stress-intensity factor (at  $t = 18$  min) predicted by the elastic-plastic analysis (using the 20-node element model) approaches the (linear-elastic)  $K_I$ -value calculated by the FAVOR code and is 8% higher than the value obtained from the 8-node element model. The linear-elastic stress-intensity factor calculated using the 20-node element model at  $t = 18$  min shows a value of 10% lower than the FAVOR prediction.

In contrast, the peak stress-intensity factor (at  $t = 18$  min) computed from the elastic-plastic analysis (using the 20-node element model) for the axially embedded crack exceeds the FAVOR prediction by 22%. The linear-elastic solutions agree well with the (LEFM) FAVOR predictions, with the peak  $K_I$ -value (at  $t = 18$  min) remaining 7% lower than the FAVOR solution. The difference between the linear-elastic solution and the elastic-plastic solution for the axially embedded crack exceeds the difference in the linear-elastic and elastic-plastic  $K_I$ -values for the circumferentially embedded crack. Comparison of the elastic-plastic solution and the FAVOR estimation for the axially embedded crack implies that the FAVOR code, with a linear-elastic assumption, can potentially under-estimate the crack driving force for RPVs under PTS.

Under the same PTS event (Transient A), the computed driving force for the axially embedded crack is much larger than that for the circumferentially embedded crack because: (1) the size of the axially embedded crack is significantly larger than the circumferentially embedded crack, as shown in Table 1, (2) the axially embedded crack resides nearer the inner surface of the RPV, and thus experiences lower temperature values along the crack front, compared to the circumferentially embedded crack, and (3) the doubled nominal wall (hoop) stress normal to the crack plane.

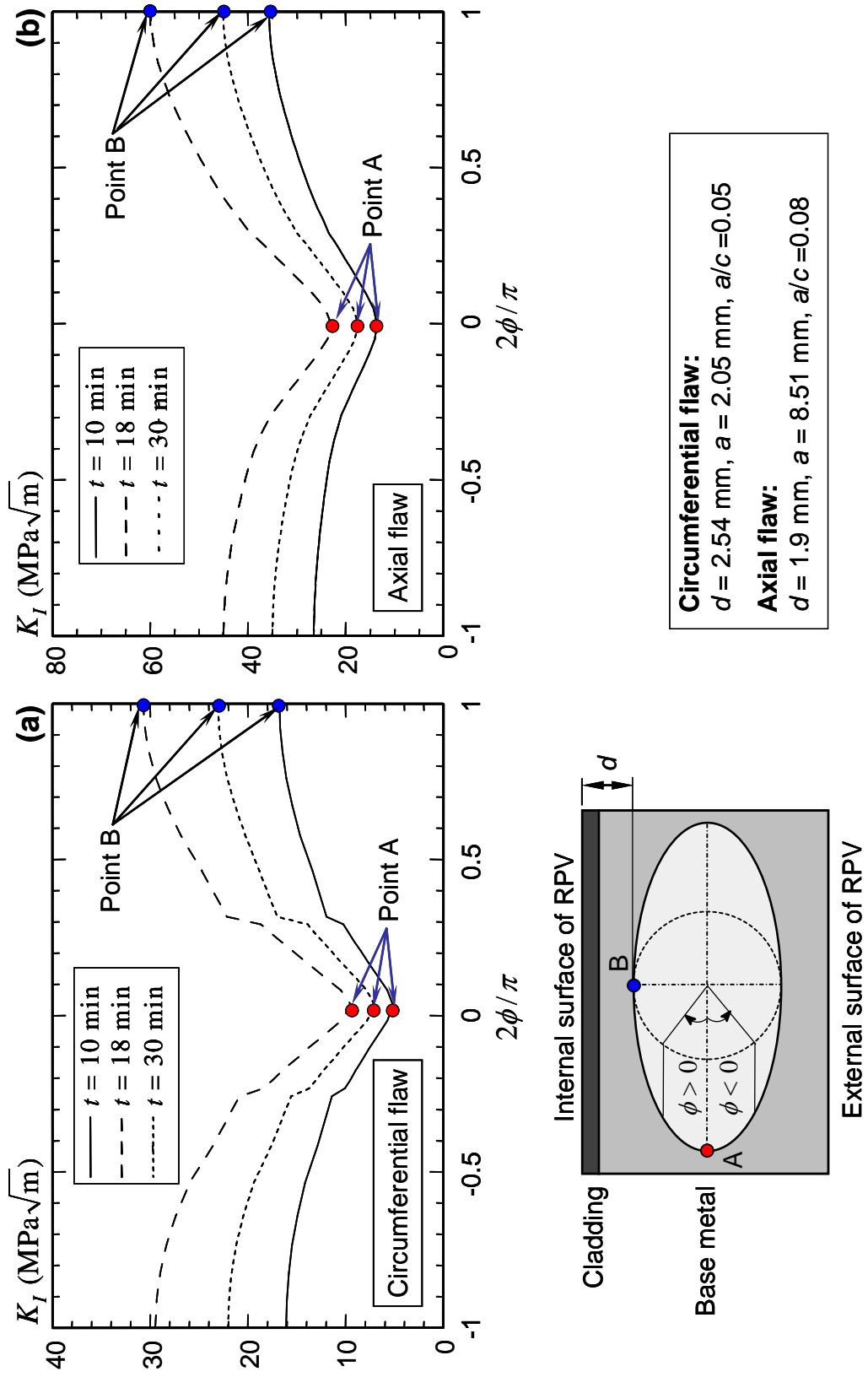


Fig. 9.  $K_I$  values along the crack front for Transient A (FE models using 8-node brick elements) with: (a) a circumferentially embedded flaw; and (b) an axially embedded flaw.

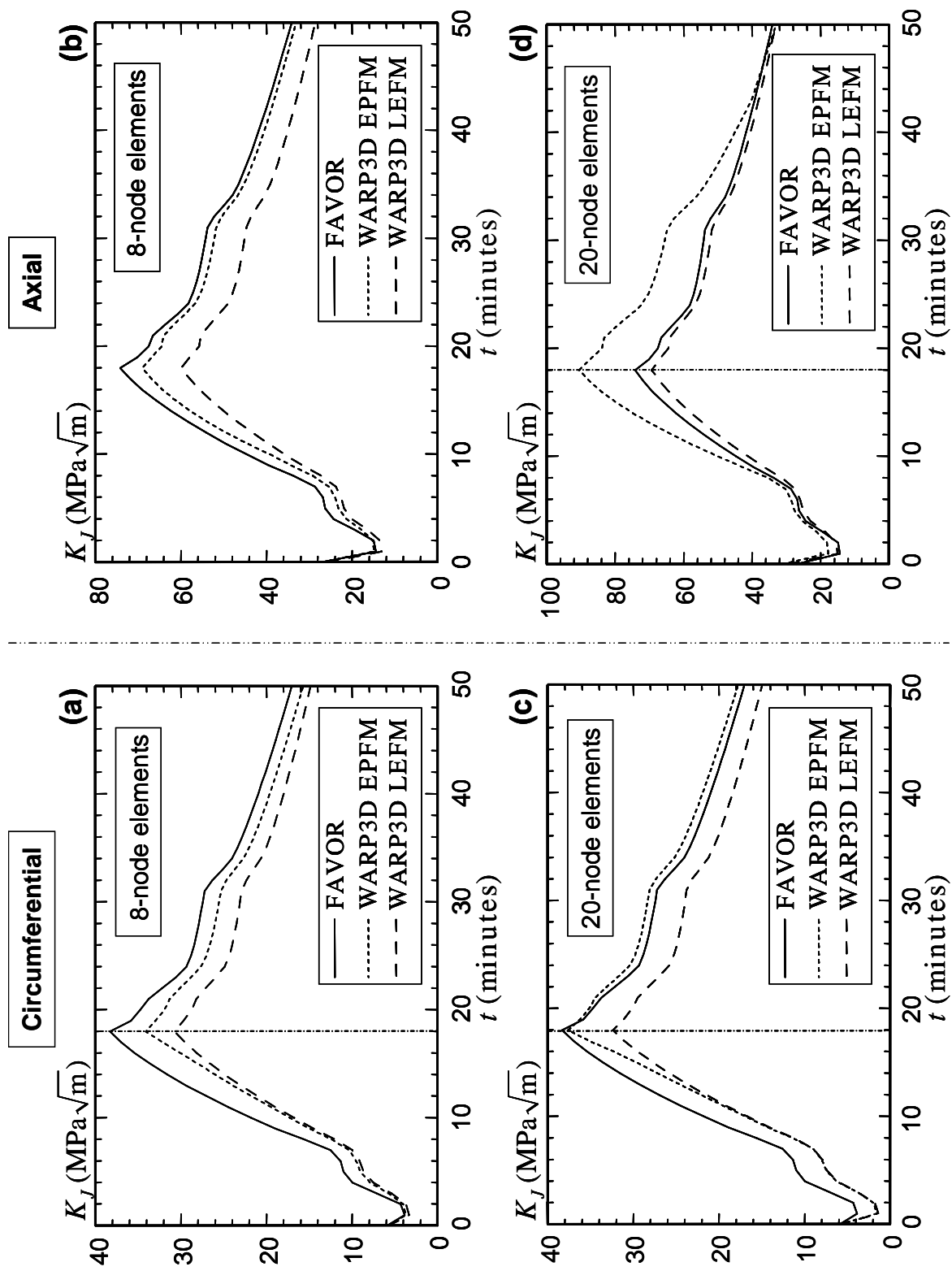


Fig. 10.  $K_I$ -time history for Transient A with: (a) a circumferentially embedded flaw using 8-node element; (b) an axially embedded flaw using 8-node elements; (c) a circumferentially embedded flaw using 20-node elements; and (d) an axially embedded flaw using 20-node elements.

## 4.2 Transient B

Figures 11a and 11b show the stress-intensity factor values over the time history computed for an axial and a circumferential flaw in the wall for Transient B using 8-node element models. For the circumferentially embedded crack shown in Fig. 11a, the combination of thermal and pressure loading generates a maximum stress-intensity factor at  $t = 31$  min based on the FAVOR prediction. The crack driving force, calculated by the FAVOR code, then decreases with time and shows a slight increase at  $t = 140$  min due to a sudden increase in the internal pressure. The WARP3D linear-elastic and the elastic-plastic solutions are lower than the FAVOR prediction for  $t \leq 100$  min, as shown in Fig. 11a. The linear-elastic crack driving force shows a maximum value at  $t = 33$  min, which is 15% lower than the peak value of the FAVOR solution. The elastic-plastic analysis shows a maximum  $K_J$ -value at  $t = 54$  min, with 13% lower than the peak value predicted by the FAVOR code. The large increase of the internal pressure at  $t = 147$  min causes a larger increase in the  $K_J$ -values in the elastic-plastic analysis than in the linear-elastic analysis. However, the  $K_J$ -values at  $t = 147$  min do not exceed the peak values obtained at time steps before the large pressure increase.

For the axially embedded crack shown in Fig. 11b, similar trends exist in the  $K_J$  solutions up to  $t = 140$  min. For  $t > 140$  min, the stress-intensity factor increases substantially due to the sudden increase in the internal pressure. The increase in the internal pressure causes a more significant impact for the axial flaw than for the circumferential flaw since the circumferential hoop stress in the wall of an RPV (due to internal pressure) acting normal to the face of the axial flaw equals approximately twice the axial stress acting normal to the face of the circumferential flaw. The stress-intensity factor thus shows a maximum value at  $t = 147$  min, with approximately twice the magnitude compared to the stress-intensity factor at  $t = 140$  min. The elastic-plastic analysis shows the highest value for the peak stress-intensity factor, with a value of 7% higher than the (linear-elastic) FAVOR solution. The WARP3D linear-elastic stress-intensity factor remains the smallest among the three analyses, with the peak value 9% lower than the FAVOR prediction.

The analyses using the 20-node element models again show higher values of stress-intensity factors for both the circumferentially embedded and the axially embedded crack compared to the solutions obtained from the 8-node element models, as illustrated in Figs. 11c and 11d. For the circumferentially embedded crack, the maximum linear-elastic stress-intensity factor occurs at  $t = 35$  min, with a 6% lower value than the FAVOR code prediction. The elastic-plastic analysis shows a peak value of 1% lower than the FAVOR solution, albeit at a later time step ( $t = 82$  min). The sudden increase in the internal pressure at  $t = 147$  min causes substantial increase in the crack driving force in all three analyses, but with the  $K_J$ -values (at  $t = 147$  min) remaining smaller than the peak values obtained before the sudden pressure increase.

The FE analyses for Transient B using the 20-node brick elements for axially embedded flaws again show higher  $K_J$ -values than the values computed with the 8-node element models. The peak stress-intensity factors from both the linear-elastic and the elastic-plastic solutions demonstrate larger values than the

FAVOR prediction at  $t = 147$  min, with the linear-elastic  $K_J$ -value 5% higher than the FAVOR solution and the elastic-plastic  $K_J$ -value 26% larger than the FAVOR solution.

As expected for all the analyses performed in WARP3D, the elastic-plastic stress-intensity factors ( $K_J$ -values) show larger magnitudes than the linear-elastic solutions. The difference between the linear-elastic and elastic-plastic solutions can be significant as shown here, especially for the axially embedded crack under PTS transient loading histories. For the axially embedded crack under both transient loadings, the elastic-plastic stress-intensity factors show  $K_J$ -values higher than the (linear-elastic) FAVOR code predictions. The magnitude of the difference does appear to be sufficient ( $\approx 20 \text{ MPa}\sqrt{\text{m}}$ ) in some cases to likely affect the assessment outcome.

The 20-node element models show a uniform prediction of larger stress-intensity factors ( $K_J$ -values) than the 8-node element models. The isoparametric, 8-node elements exhibit shear locking behavior under bending-type deformations induced by the local, thermal gradients over the wall thickness of an RPV. The 8-node element model exhibits an overly stiff response, and leads to computation of a lower driving force along the curved crack front for RPVs under PTS. The extensive mesh refinement here, with more than 50 layers of elements across the wall thickness, does not improve the performance of the 8-node elements. The isoparametric, 20-node elements alleviate the shear-locking behavior and predict higher (and more realistic)  $K_J$ -values than the 8-node elements.

The differences in  $K_J$ -values observed here for models constructed with 8 and 20 node elements are unexpected. The 8-node element meshes have extensive refinement (84,000 elements), yet the 20-node element meshes used here have far more extensive refinement (20,000 elements) than were used in much earlier studies to compute the weight function values incorporated into FAVOR. This likely is the key source of the usually (small) difference shown in Figs. 10 and 11 between the FAVOR  $K_J$ -values and the corresponding linear-elastic values from the 20-node element meshes shown here.

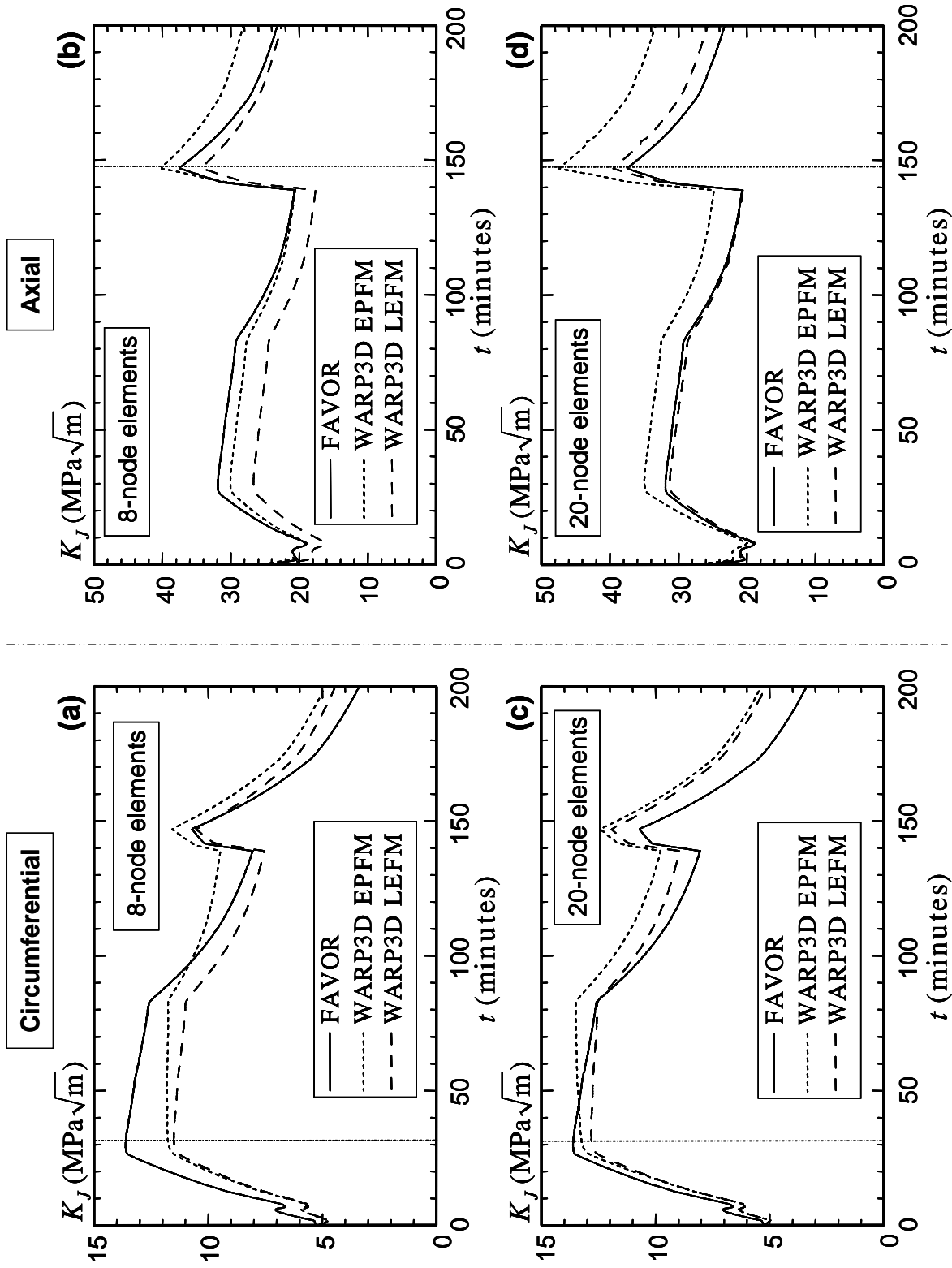


Fig. 11.  $K_J$ -time history for Transient B with: (a) a circumferentially embedded flaw using 8-node elements; (b) an axially embedded flaw using 8-node elements; (c) a circumferentially embedded flaw using 20-node element; and (d) an axially embedded flaw using 20-node elements.

### 4.3 Plastic Material Response Under PTS

The larger elastic-plastic  $K_J$ -values, compared to the linear-elastic solutions, indicate the influence of plastic deformations near the front of the axial and the circumferential crack, especially at the time of high temperature gradients across the wall thickness and/or internal pressures. In addition to plastic deformation near the crack front, the mismatch in yield strength of the base and cladding materials creates a potential effect on the nearby crack-front fields.

To illustrate this, Fig. 12 shows fringe plots of the Mises (equivalent) stress normalized by the yield stress of the base material at the peak stress-intensity value ( $t = 18$  min) for the axially embedded crack under Transient A. These results are obtained from the model using 20-node elements. Due to the different material properties for the base and cladding steels and nonlinear response, the elastic-plastic analysis exhibits markedly different stress distributions, compared to the linear-elastic analysis (which reflects only an elastic modulus and CTE mismatch). For the elastic-plastic analysis, significant plastic deformation develops in the base material as well as in the cladding material near the inner surface of the RPV ( $\sigma_{ys}^{base} \approx 3\sigma_{ys}^{cladding}$ ). In the linear-elastic analysis, values of the Mises stress in the cladding material exceed three times the yield stress of the austenitic steel. The artificial, linear-elastic behavior of the cladding material supports substantial additional forces, and thus shields the nearby base material, which otherwise experiences a significant plastic deformation in the elastic-plastic analyses. Consequently, the crack driving forces show lower values in the linear-elastic analyses, compared to the elastic-plastic analyses.

The difference in properties of the ferritic and austenitic steels causes substantially different stress fields in the base and cladding materials under linear-elastic and elastic-plastic analyses. The linear-elastic analysis computes unrealistically high stress values in the cladding material, which consequently affects the stress fields in the base material, and produces unrealistic, lower values of the crack driving force. In contrast, the elastic-plastic analysis properly incorporates the effects of the very low yield strength of the cladding material, and computes a more realistic stress field near the crack front and thus more realistic  $K_J$ -values.

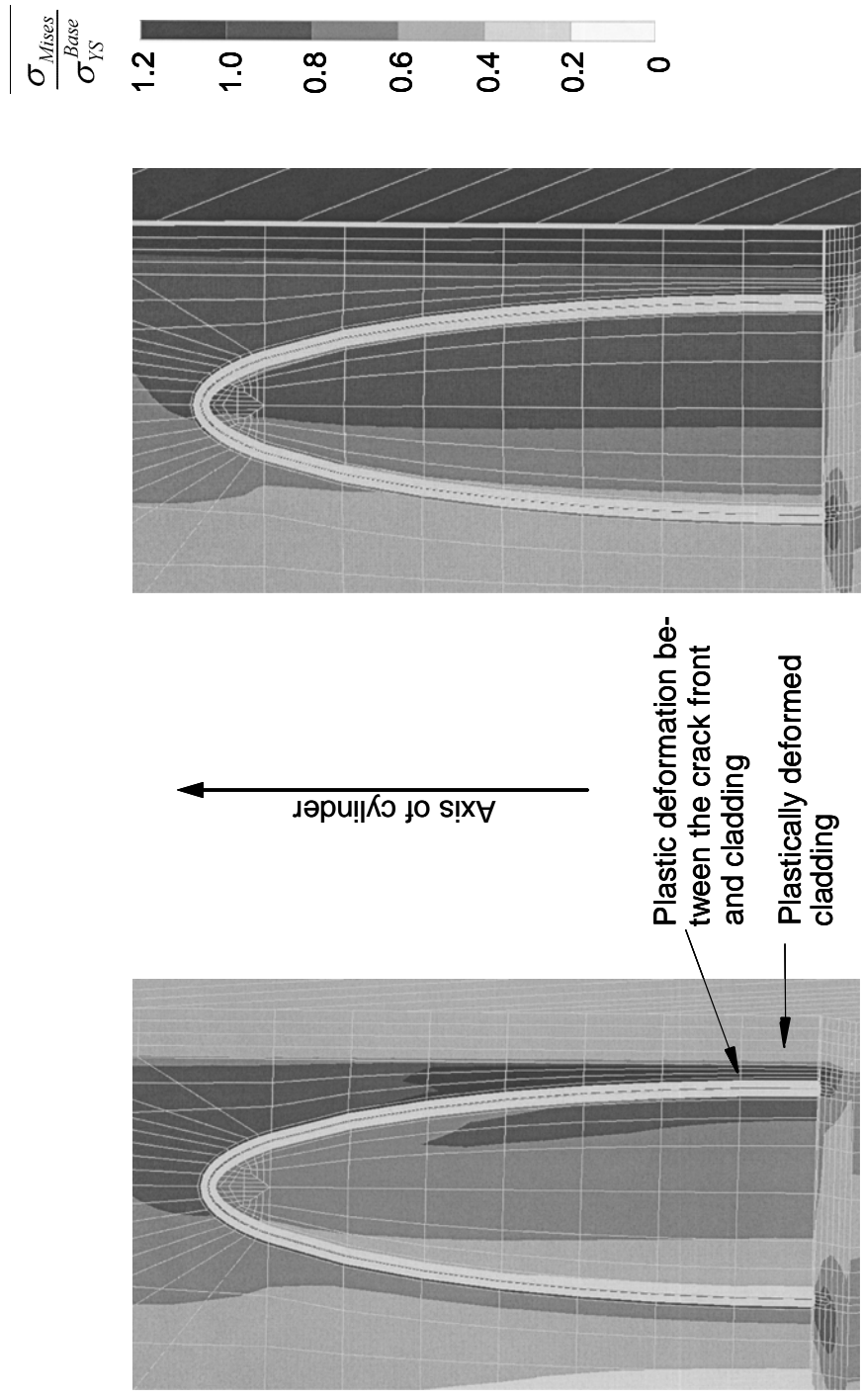


Fig. 12. The fringe plot of Mises equivalent stress for Transient A imposed on an axially embedded flaw, computed using 20-node brick elements at  $t = 18$  min.

This page is intentionally blank.

## 5 Weibull Stress Approach

---

### 5.1 Weibull Stress Values for RPVs Under PTS

The region between the cladding material and the axially embedded crack for Transient A develops significant plastic deformation under a pressurized thermal shock event as demonstrated by the fringe plots in Fig. 12. The potential process zone for cleavage fracture in the base material is therefore larger in volume for the elastic-plastic analysis and is subjected to larger local, loading levels than predicted by the linear-elastic analysis. The larger fracture process zone and loading levels increase the probability of cleavage fracture failure. The Weibull stress approach provides a framework to characterize the effects of plastic deformation coupled with potential constraint loss from the proximity of the crack front to the inner wall of the vessel.

The effective stress,  $\sigma_{eff}$ , acting on material within the process zone represents a local driving force that triggers the propagation of microcracks. Different micro-scale criteria for cleavage (*e.g.*, the coplanar energy release rate criterion and the maximum principal stress  $\sigma_1$ -criterion) yield different definitions of the effective stress [23]. The  $\sigma_{eff} = \sigma_1$  approach implies that the most favorably oriented carbide particle aligns in the direction of  $\sigma_1$  and that imposes the most likely loading to propagate the microcrack associated with the particle. The most commonly used definition of the Weibull stress adopts the maximum principal stress,  $\sigma_1$ , as the effective stress. Williams *et al.* [47] adopt the hydrostatic stress,  $\sigma_H = (\sigma_1 + \sigma_2 + \sigma_3)/3$ , as the effective stress, rather than the maximum principal stress. They demonstrate that  $\sigma_{eff} = \sigma_1$  fails to correlate the cumulative failure probability between biaxially loaded bend and conventional bend specimens, *i.e.*, biaxial bend specimens have a high level of mechanically imposed stress parallel to the (through) crack front. A shallow-notch, biaxial bend specimen thus imposes crack-front loading that more closely represents the crack-front loading in an RPV.

To compare different definitions of  $\sigma_{eff}$  in engineering applications of the Weibull stress approach for RPVs under PTS, the current study computes the Weibull stress using  $\sigma_H$  and  $\sigma_1$ , respectively. The characteristic “cutting stress” parameter,  $\lambda$ , which determines the effective volume of the fracture process zone, takes four typical values between 1.5-2.7 for  $\sigma_{eff} = \sigma_1$  ( $\lambda = \sigma_1 / \sigma_0$ ), and four values between 1.25-2 for  $\sigma_{eff} = \sigma_H$  ( $\lambda = \sigma_H / \sigma_0$ ). Material volumes in the crack-front region with effective stress values below the cutoff value do not enter into the computed value for  $\sigma_w$ . The  $\lambda$  value thus imposes a “threshold” parameter in the Weibull stress model. Ideally, the calibrated exponent,  $m$ , for a material effectively eliminates or minimizes any impact of  $\lambda$  on the  $\sigma_w$  values, *i.e.*, for  $\sigma_{eff} = \sigma_1$  and  $m > 12-15$ , the typical values for  $\lambda$  make no difference on  $\sigma_w$  values [28]. Large values of exponents ( $m$ ) severely limit the influence of stress levels below the maximum value ahead of the crack front (*e.g.*, compare the value of  $0.9^{15} = 0.21$  relative to  $1^{15} = 1.0$ ).

The current study calculates the Weibull stress values for the 20-node element model of an axially embedded crack under Transient A, since this configuration demonstrates the highest crack driving force among the four cases investigated. Figure 13 compares the Weibull stress values computed using

$\sigma_{eff} = \sigma_1$  over a typical range of values for  $m$  and  $\lambda$ . A larger value of  $\lambda$  reduces the volume of the fracture process zone,  $V_f$  (in Eq. 10). At high values of  $\lambda$  ( $\geq 2.5$ ), the computed Weibull stress remains at zero well into the PTS event, as demonstrated in Figs. 13c and 13d. The effective stress remains below the  $\lambda$ -imposed threshold. For the smaller  $\lambda$  values ( $\leq 2.0$ ), the calculated Weibull stresses show negligible differences among different  $\lambda$  values for the same Weibull modulus,  $m$ , as illustrated in Figs. 13a and 13b. The difference in the computed Weibull stress values for low  $\lambda$ -values decreases with increasing  $m$  — a higher value of  $m$  promotes the contribution to  $\sigma_w$  of high stress material very near the crack tip. A too large value of the cutting stress parameter for a low  $m$ -value underestimates the Weibull stress values and subsequently the cumulative probability of fracture. For Transient A with  $\sigma_{eff} = \sigma_1$ , the Weibull stress (computed using the same value of  $m$ ) remains approximately the same for  $\lambda$  below 2. The maximum difference between the Weibull stresses using  $\lambda = 1.5$  and  $\lambda = 2$  equals 3% for a small value of  $m$  ( $=10$ ), and remains less than 1% for  $m \geq 15$ .

Similar trends exist for the calculated Weibull stress values with  $\sigma_{eff} = \sigma_H$ , as illustrated in Fig. 14. At a large value of  $\lambda$  ( $=2$ ), the Weibull stress equals 0 until  $t = 13$  min. For  $\lambda \leq 1.5$ , the computed Weibull stress values remain approximately the same for different  $\lambda$  values, especially at larger values of  $m$ . The maximum difference between the Weibull stresses calculated using  $\lambda = 1.25$  and  $\lambda = 1.5$  equals 2% for a small value of  $m$  ( $=10$ ), and remains much less than 1% for  $m \geq 15$ . Compared to the definition of  $\sigma_{eff} = \sigma_1$ , the definition of  $\sigma_{eff} = \sigma_H$  reduces significantly the Weibull stress values. For the axially embedded crack, the value of Weibull stress computed using  $\sigma_{eff} = \sigma_H$  at  $\lambda = 1.5$  remains 25-30% lower than the Weibull stress with  $\sigma_{eff} = \sigma_1$ , for different values of  $m$ . These large differences in the Weibull stress values for  $\sigma_{eff} = \sigma_1$  and  $\sigma_{eff} = \sigma_H$  must necessarily then lead to different calibrated values of  $m$  and  $\sigma_u$ . However, no definitive study yet exists to investigate the definitions of  $\sigma_{eff}$  on the calibrated Weibull stress parameters.

For both choices of  $\sigma_{eff}$ , the Weibull stress reaches the maximum value at  $t = 18$  min, corresponding to attainment of the maximum crack driving force ( $K_J$ ), see Fig. 10d. Both of these definitions for the effective stress provide the same trend of Weibull stress evolution over the time history. A large value of  $\lambda$  may lead to underestimated Weibull stress values, especially in the initial stage of the PTS, where the Weibull stress equals zero for  $\sigma_{eff} = \sigma_1$  with  $\lambda \geq 2.5$  and for  $\sigma_{eff} = \sigma_H$  with  $\lambda \geq 2$ . For  $\sigma_{eff} = \sigma_H$ , the Weibull stress reaches a stabilized value with respect to  $\lambda$  for a relatively large volume of the fracture process zone ( $\lambda = 1.5$ ), compared to the case where  $\sigma_{eff} = \sigma_1$  ( $\lambda = 2$ ).

The definition of the effective stress and the variation of cutting stress parameters change the Weibull stress values which, combined with the Weibull stress parameters  $m$  and  $\sigma_u$ , determine directly the cumulative probability of failure. As an example, the Weibull stress (with  $\sigma_{eff} = \sigma_1$ ) equals  $1.7\sigma_{ys}$  for  $\lambda = 2$  and  $1.6\sigma_{ys}$  for  $\lambda = 2.5$ , for a typical Weibull modulus of  $m = 15$ . The cumulative probability of failure calculated from a simple two-parameter Weibull stress model ( $P_f = 1 - \exp[-(\sigma_w / \sigma_u)^m]$ , or Eq. 9) equals  $P_f(\sigma_w = 1.7\sigma_{ys}) = 8.3\%$  and  $P_f(\sigma_w = 1.6\sigma_{ys}) = 3.5\%$ , with an assumed, typical value of  $\sigma_u = 2\sigma_{ys}$ . However, the cumulative probability of failure also exhibits sensitivity to the Weibull scaling parameter,  $\sigma_u$ . For the same example with a slightly different value of the Weibull scaling parameter,  $\sigma_u = 1.9\sigma_{ys}$ ,

$P_f(\sigma_w = 1.7\sigma_{ys}) = 17.2\%$  and  $P_f(\sigma_w = 1.6\sigma_{ys}) = 7.3\%$ . Therefore, different definitions of the effective stress and the change in the cutting stress parameter can cause potentially significant variations in the cumulative probability of failure.

## 5.2 Estimation of Weibull Stress Parameters

Engineering applications of the Weibull stress approach require the calibration of three Weibull stress parameters: the Weibull modulus,  $m$ , the Weibull scaling parameter,  $\sigma_u$ , and the threshold Weibull stress,  $\sigma_{w-min}$ . Previous investigations [21, 39, 40, 46] introduce new schemes to calibrate unique values of the key Weibull stress parameter, the modulus  $m$ . The most correct calibration procedure requires testing a set of high constraint fracture specimens and a set of low constraint fracture specimens at a common temperature, combined with detailed, nonlinear 3-D finite element analyses of the specimens to compute the evolution of  $\sigma_w$ -values with loading. The calibrated value of  $m$  then minimizes an error function which quantifies the difference in fracture toughness values,  $K_{Jc}$ , scaled for constraint variations from the high and low constraint specimens to a common, SSY configuration (often with  $T_\sigma = 0$ ). This same fracture testing also generates the reference temperature,  $T_0$ , for the material for subsequent use to help calibrate  $\sigma_u$ .

The current calibration methodology adopts a constant value of the exponent,  $m$ , over the ductile-to-brittle transition region of temperatures. The recent work of Wasiluk *et al.* [40] validates this assumption for a common RPV steel. With  $m$  known,  $\sigma_u$  represents the key remaining Weibull stress parameter. In the Weibull stress micromechanical model,  $\sigma_u$  plays the same role as  $K_0$  in the macroscopic model described and adopted in ASTM E-1921. With  $m$  taken as invariant of temperature,  $\sigma_u$  must vary with temperature just as  $K_0$  varies with temperature.

ASTM E-1921 [29] employs an empirically developed Master Curve to describe the relationship of the median fracture toughness ( $P_f = 0.5$ ) with respect to temperature for a 1T specimen size (*i.e.*, crack-front length equals 25 mm),

$$K_{Jc}^{1T} = 30 + 70 \exp[0.019(T - T_0)] \text{ MPa}\sqrt{\text{m}}, \text{ } ^\circ\text{C} \quad (13)$$

where  $T_0$  defines the temperature at which the median toughness for a 1T size specimen equals 100  $\text{MPa}\sqrt{\text{m}}$ . Petti and Dodds [28] couple the micromechanical approach in terms of the local stress parameter,  $\sigma_w$ , and the macromechanical approach in terms of the elastic-plastic far field loading,  $K_J^{1T}$ . They relate the Weibull scaling parameter  $\sigma_u$  to the macroscopic scaling parameter  $K_0^{1T}$ , which derives from the unnormalized Master Curve and knowledge of  $T_0$  for the material (found from tests to calibrate  $m$ ),

$$K_0^{1T} = 31 + 77 \exp[0.019(T - T_0)] \text{ MPa}\sqrt{\text{m}}, \text{ } ^\circ\text{C}. \quad (14)$$

The relationship between the Weibull stress and the  $K_J$ -values follows from finite element analyses of the laboratory test specimens. Since Eq. 12 remains equivalent to the macromechanical approach described in E-1921 for SSY ( $T_\sigma \geq 0$ ) conditions, the Weibull scaling parameter,  $\sigma_u$ , thus equals

$\sigma_u = \sigma_w(K_J = K_0^{1T})$  for SSY conditions. Petti and Dodds [39] adopt this relationship to calibrate  $\sigma_u$  over the ductile-to-brittle transition temperatures for an A508 steel. In a subsequent work, Wasiluk *et al.* [40] first calibrate the values of  $m$  and  $K_{min}$  based on a set of high constraint test data and a set of low constraint test data. The values for  $\sigma_u$  and  $\sigma_{w-min}$  in Eq. 12 then follow the relationship between  $\sigma_w$  and  $J$ , or simply  $\sigma_u^{1T,SSY} = \sigma_w^{1T,SSY}(K_0^{1T})$  and  $\sigma_{w-min}^{1T,SSY} = \sigma_w^{1T,SSY}(K_{min}^{1T})$ . The application of their approach on the Eurodataset [42] proves to be successful in predicting the probability of failure over a wide range of temperatures in the ductile-to-brittle transition.

The coupling of microscopic Weibull stress and the macroscopic crack driving forces, together with the existing, verified calibration procedures for the Weibull stress parameters, forms a theoretical basis for the practical application of the Weibull stress procedure in assessments of cleavage fracture in RPVs under PTS. In the next section, we propose two procedures for the PTS assessment which employ these coupling and calibration procedures.

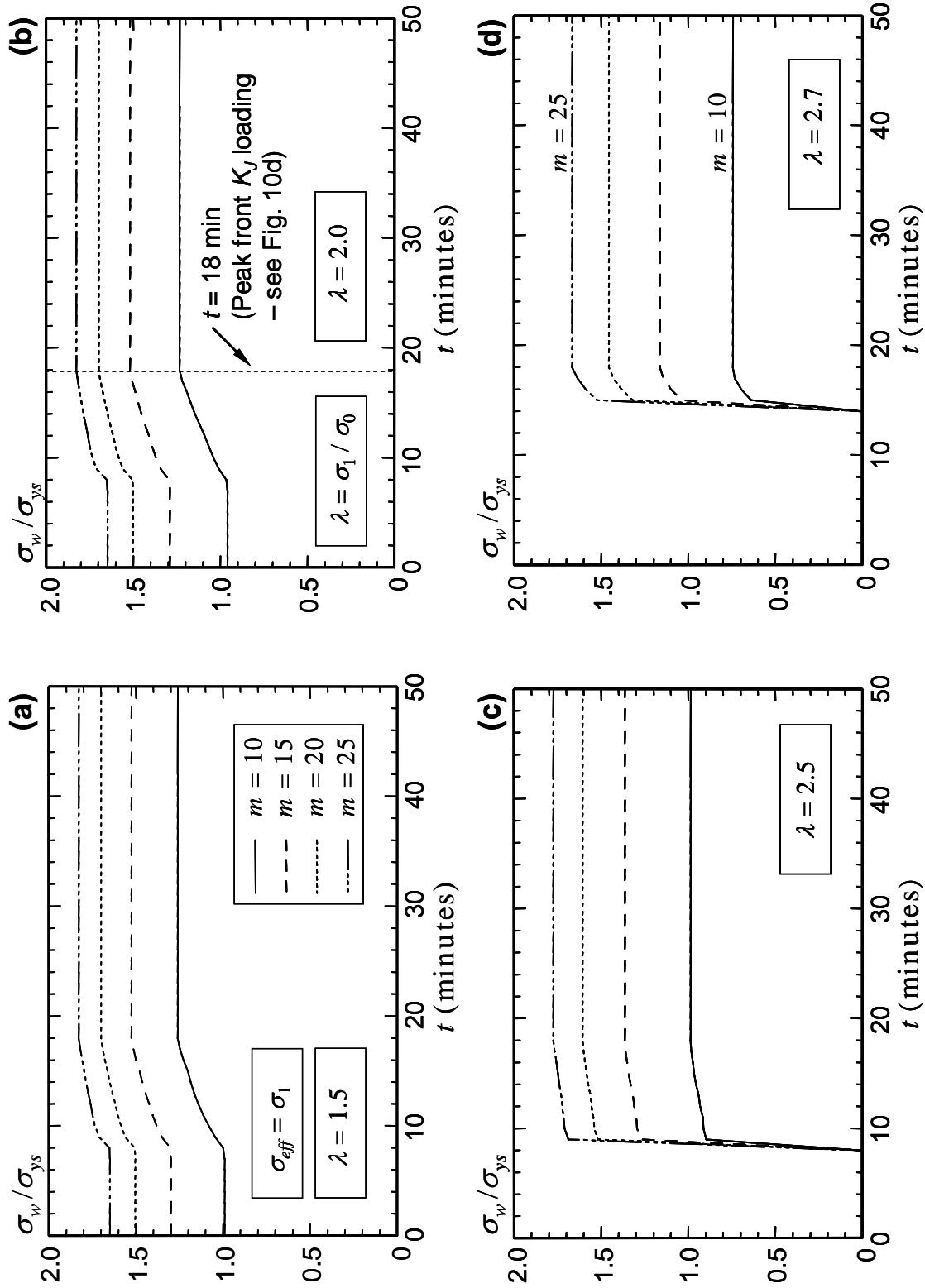


Fig. 13. Weibull stress variation over time history for an axially embedded flaw subjected to Transient A (20-node element model) with  $\sigma_{eff} = \sigma_1$  and: (a)  $\lambda = 1.5$ ; (b)  $\lambda = 2.0$ ; (c)  $\lambda = 2.5$ ; and (d)  $\lambda = 2.7$ .

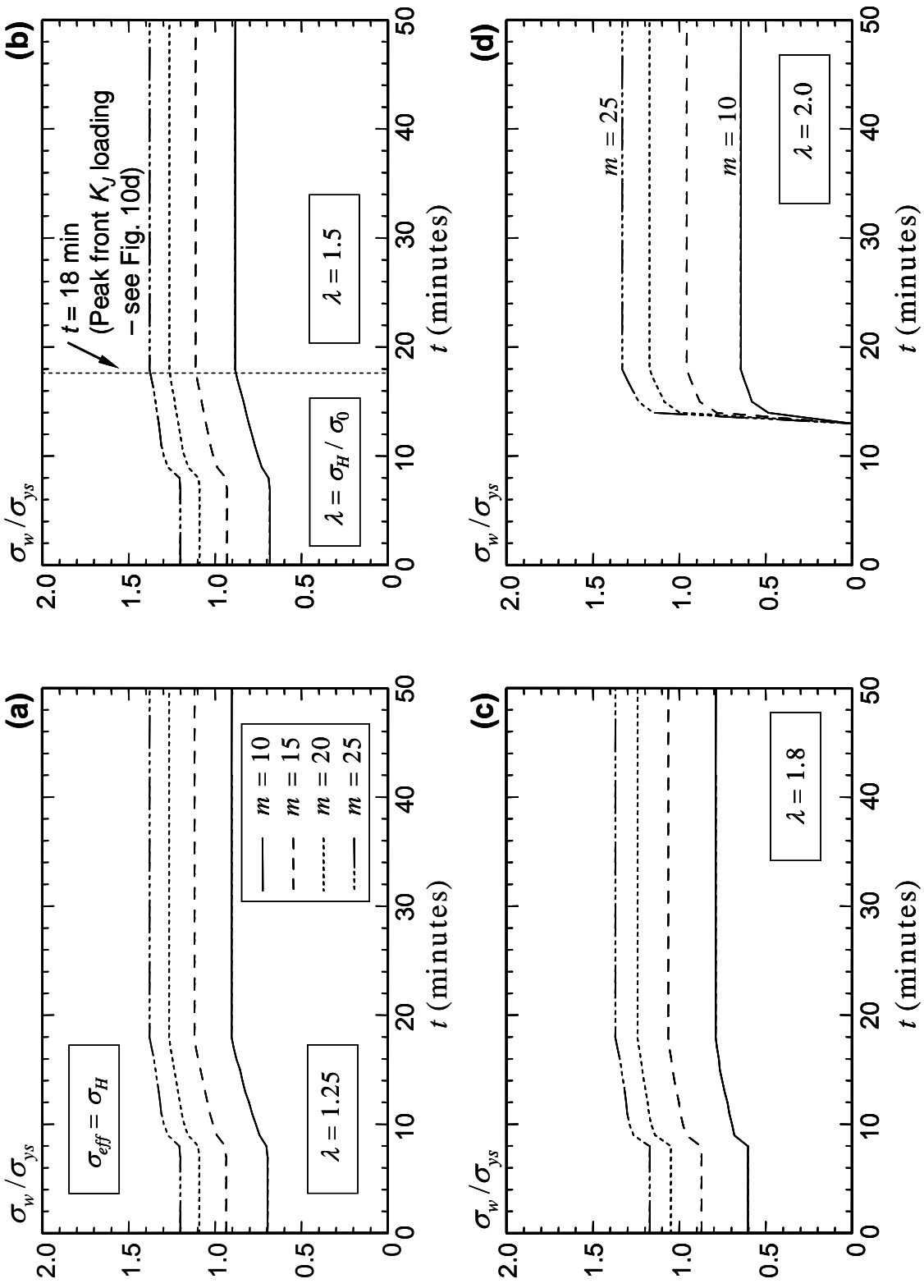


Fig. 14. Weibull stress variation over time history for an axially embedded flaw subjected to Transient A (20-node element model) with  $\sigma_{eff} = \sigma_H$  and: (a)  $\lambda = 1.25$ ; (b)  $\lambda = 1.5$ ; (c)  $\lambda = 1.8$ ; and (d)  $\lambda = 2.0$ .

## 6 Application of Local Approach to PTS Assessment

---

### 6.1 Complications for RPVs

In typical research applications of the Weibull stress framework conducted to date, the laboratory specimens have relatively straight, through-thickness cracks with constant temperature at all locations along the front. Consequently, the Weibull stress parameters,  $\sigma_u$  and  $\sigma_{w-min}$ , and material flow properties remain constant at all crack-front locations. Local  $K_J$ -values along the crack front remain relatively uniform except for much lower values over the thin boundary layer transition at the outside surface of the specimens. The 3-D finite element analyses that accompany these tests readily yield a thickness average  $K_J$ -value and the corresponding (single)  $\sigma_w$ -value at each level of applied loading. The  $K_J$ -value corresponds to the value found using the measured  $P-\Delta_{CMOD}$  curve and an  $\eta$ -value for the specimen configuration, or through direct, 3-D finite element analysis of the specific specimens. Experimental and computational studies using the measured  $K_{Jc}$ -values and corresponding  $\sigma_w$ -values are thus greatly simplified by the constant  $\sigma_u$  and  $\sigma_{w-min}$  values, and flow properties along the crack front.

The conditions for an embedded crack in the wall of an RPV under time-dependent, thermal-mechanical loadings become far more complex. The temperature, and thus  $\sigma_u$  and  $\sigma_{w-min}$ , can vary significantly along the crack front. Similarly,  $\sigma_u$ ,  $\sigma_{w-min}$  and flow properties likely also vary along the crack front from differing levels of material damage caused by accumulated radiation exposure over years of service life. This potentially strong variation in local fracture and flow properties along the crack front, coupled with strong variations in crack-front loading of the type computed here (see Fig. 9) leads to a very complex situation to apply the Weibull stress framework (or any other framework). In essence, each segment of material along the front of an embedded crack is effectively a small “component” with its own loading history and time varying flow and toughness properties ( $\sigma-\varepsilon$ ;  $K_0$ ,  $\sigma_u$  and  $\sigma_{w-min}$ ). The assumption (now apparently validated) of temperature invariant exponent,  $m$ , does provide some much needed simplification.

This section describes three approaches to apply the Weibull stress framework for PTS assessments under these complex conditions. The first “refined” approach represents the most complicated method and incorporates the most detailed analysis and calibrations of material parameters. The second approach adopts a uniform material toughness (at the lowest temperature along the front) for the entire crack front to simplify the process. In the third approach, the nonlinear 3-D analysis of the RPV is replaced by a linear-elastic  $K_I-T$  solution over the loading history coupled with 2-D, SSY boundary layer models (driven by the  $K_I-T$  values) to generate the evolution of Weibull stress values over the PTS transient.

### 6.2 A Refined Procedure of PTS Assessment for RPVs

The variation of temperature along the front of an embedded crack likely causes significant spatial and temporal changes in both the material properties and the local crack driving force, which require detailed mathematical descriptions for an accurate estimation of the cumulative probability of failure. The thermal loading varies the mechanical properties of the material along the crack front and introduces a strong im-

impact on the Weibull scaling parameter,  $\sigma_u$ , and a small impact on the threshold Weibull stress,  $\sigma_{w-min}$ . Meanwhile, the local Weibull stress may change significantly along the crack front, as demonstrated by the variation of the macroscopic crack driving force  $K_J$  in Fig. 9. To include the variation of material properties along the crack front, a refined procedure for PTS assessment divides material along the entire crack front into  $n$  small subregions each with length  $c_{(i)}$  ( $i=1, 2, \dots, n$ ). Each subregion thus experiences a spatially constant temperature and a spatially constant loading  $K_{J_{(i)}}$ . The total cumulative failure probability follows as,

$$P_f^{Total}(t_k) = 1 - \exp \left[ - \sum_{i=1}^n \left( \frac{\sigma_{w_{(i)}}^{m/4} - \sigma_{w-min_{(i)}}^{m/4}}{\sigma_{u_{(i)}}^{m/4} - \sigma_{w-min_{(i)}}^{m/4}} \right)^4 \right], \quad (15)$$

where  $\sigma_{u_{(i)}}$  and  $\sigma_{w-min_{(i)}}$  denote the Weibull scaling parameter and the threshold Weibull stress parameter of the subregion  $i$ . Equation 15 defines the total, cumulative failure probability of the embedded flaw in the RPV at a specific time  $t_k$  of the transient.

The following steps describe the procedure which incorporates the variation of the thermal and mechanical material responses along the entire crack front, and operates on predefined subregions to predict the total cumulative failure probability.

1. For an RPV with a designated flaw size and location, determine the temperature variation along the curved, 3-D crack front at times of interest during the PTS transient.
2. Using the procedure described in the Appendix, calibrate the temperature independent Weibull modulus ( $m$ ) for the base material of the RPV. Compute values of  $\sigma_u$  and  $\sigma_{w-min}$  at selected, representative values of the temperature experienced along the crack front, at times of interest during the PTS event.
3. Perform a detailed 3-D, nonlinear analysis of the flawed RPV, including temperature dependent flow properties for the base material. Compute the macroscopic crack driving force ( $K_J$ ) along the crack front (as exemplified in Fig. 9) for each time increment of the PTS transient. Divide the material along the crack front into  $n$  subregions based on the temperature variation (determined in step 1) and the variation of  $K_J$ -values along the crack front, such that each subregion experiences a spatially constant temperature and the spatially constant,  $K_{J_{(i)}}$ .
4. Compute the Weibull stress value,  $\sigma_{w_{(i)}}$ , within each segment along the crack front, for every time increment of the PTS transient using the calibrated  $m$  (or a range of values for a sensitivity study). The computed Weibull stress reflects a "history" effect, *i.e.*,  $\sigma_{w_{(i)}}$  is not permitted to decrease below an earlier (larger) value during the PTS event.
5. At the time of interest, insert the computed  $\sigma_{w_{(i)}}$  and calibrated  $\sigma_{u_{(i)}}$  and  $\sigma_{w-min_{(i)}}$  values for each subregion along the crack front into Eq. 15 to compute the cumulative probability of failure ( $P_f$ ) for the embedded crack at that time during the PTS event.
6. Repeat step 5 for a new (increased) time during the PTS transient.

Examples of this refined approach will appear in future work.

### 6.3 A Simplified Procedure of PTS Assessment

Without using detailed evaluations of the varying (temperature dependent) Weibull stress parameters along the front of an embedded crack, the proposed simplified procedure first identifies the (critical) crack-front location with the smallest  $\sigma_u$ -value (corresponding to the lowest temperature and thus the lowest microcrack toughness value). The simplified procedure then adopts calibrated (or a range of) values of  $m$  and  $\sigma_{w-min}$  to compute the cumulative probability of fracture for the entire crack front but using the Weibull scaling parameter only at the critical location. This approach likely yields a conservative estimate for the cumulative probability of failure (to be confirmed in future work by comparison with the “refined” approach).

The following steps detail the proposed simplified procedure for RPVs under PTS,

1. For an RPV with a designated flaw size and location, identify the location with the lowest temperature along the 3-D crack front, denoted as location  $P_{crit}$  for discussion. This location usually resides near the inner surface of the RPV (point B in Fig. 9 for example).
2. Using the procedure described in the Appendix, calibrate the temperature independent Weibull modulus ( $m$ ) for the base material of the RPV. Compute values of  $\sigma_u$  and  $\sigma_{w-min}$  at selected values of the temperature experienced at  $P_{crit}$ .
3. Perform a detailed 3-D, nonlinear analysis of the flawed RPV. Compute the Weibull stress value,  $\sigma_w$ , at each time increment of the PTS transient for the full crack-front length using the calibrated  $m$  (or a range of values for a sensitivity study). The nonlinear analysis uses temperature dependent flow properties for the material. The computed Weibull stress reflects a “history” effect, *i.e.*,  $\sigma_w$  is not permitted to decrease below an earlier (larger) value during the PTS event. These results are in the form of Fig. 13.
4. For a time during the PTS transient, insert the computed  $\sigma_w$  and the calibrated  $\sigma_u$  and  $\sigma_{w-min}$  value into Eq. 12 to compute the cumulative probability of failure ( $P_f$ ) at that time during the PTS event.
5. Repeat step 4 for a new (increased) time during the PTS transient.

Figure 15 illustrates this simplified assessment procedure for the axial flaw analyzed in this study under Transient A. To compute the cumulative probability of fracture for a real, 3-D curved flaw under PTS, the calibration procedure computes the denominator of Eq. 12 through a SSY configuration. The constant  $C$  (normalized by the  $C$  value at  $K_{min} = 20\text{MP}\sqrt{\text{m}}$ ) shown in Fig. 15a defines the relationship between the far-field  $K_J$  and the local Weibull stress, or  $\sigma_w^m = CBK_J^4$  ( $B$  = crack front length), obtained from an ideal, plane-strain SSY reference configuration ( $T_\sigma = 0$ ), with assumed values of  $m$  and  $V_0 = 1.64 \times 10^{-5} \text{ m}^3$  (or  $1 \text{ in}^3$ ). As large  $m$ -values promote the contribution of high stresses to  $\sigma_w$ , the plateau magnitude of  $C$  (at large  $K_J$ -values) shows a large increase for increased  $m$ -values compared to the  $C$  value at a relatively low crack driving force,  $K_{min}$ . With  $C$  computed from the SSY model, the Weibull scaling parameter (shown in Fig. 15b) at different temperatures of the transient follows  $\sigma_u = \sigma_w(K_0)$ , where  $K_0$  is determined using Eq. 14 with the temperature at  $P_{crit}$  along the front of the axially embedded flaw in Transient A and an assumed value of  $T_0 = 130 \text{ }^\circ\text{C}$  for aged RPV steels reflecting radiation embrittlement. The threshold Weibull stress,  $\sigma_{w-min}$ , follows the  $\sigma_w - K_J$  relationship determined from the SSY model, corre-

sponding to a fixed value of  $K_{min} = 20\text{MPa}\sqrt{\text{m}}$ . Figure 15b compares  $\sigma_u$  values (normalized by the material yield strength) determined using different  $m$  values with respect to temperature at the critical crack-front location  $P_{crit}$ . A small  $m$  defines a small  $\sigma_u$  value and consequently yields a higher probability of fracture as shown in Fig. 15c, which illustrates the cumulative probability of fracture computed using Eq. 12 for the axially embedded flaw. As indicated in Fig. 13, the Weibull stress remains unchanged beyond the occurrence of the maximum crack driving force (at  $t = 18$  min) since the Weibull stress computation includes the effect of loading history on  $\sigma_{eff}$  and does not allow decreases in magnitude below a previously larger value. The temperature dependent  $\sigma_u$ -value therefore causes the variation in the cumulative probability shown in Fig. 15c beyond the occurrence of the maximum crack driving force (see Fig. 4 that shows a monotonically decreasing temperature over the vessel wall). Figure 15d illustrates the sensitivity of  $P_f$  (calculated through Eq. 12) with respect to  $\sigma_u$  for fixed values of  $\sigma_w$  (as for the  $\sigma_w$ -value beyond the peak crack driving force in the axially embedded flaw shown in Fig. 13) and  $\sigma_{w-min}$  (as in the current example,  $\sigma_{w-min} = \sigma_w(K_{min})$ , where  $K_{min}$  remains fixed at  $20\text{MPa}\sqrt{\text{m}}$ ). The cumulative probability of fracture demonstrates strong sensitivity to the  $\sigma_u$ -value, especially in cases where  $\sigma_u$  and  $\sigma_{w-min}$  are of similar magnitudes. However, variations in the  $\sigma_{w-min}$  value do not affect significantly the cumulative probability failure for fixed values of  $\sigma_w$  and  $\sigma_u$ . For the assumed values of  $m$  and a large  $T_0$ , the cumulative probability of fracture remains small ( $< 2.5\%$ ) for this large flaw size, location and orientation in the RPV with the measured material properties and postulated transients.

The simplified procedure ignores variations of the crack driving force and material properties along the curved, 3-D crack front. Warm prestress effects are also ignored in this example calculation but can be included in a more complex assessment. This approach is relatively simple and may lead to a conservative approach (higher  $P_f$ ) for the failure assessment for RPVs under PTS, by applying the smallest  $\sigma_u$  to the entire crack front.

#### 6.4 $K_I$ - $T$ Approximation for Nonlinear Crack-Front Fields

The full 3-D, elastic-plastic analysis of the RPV model containing an embedded flaw provides the most realistic estimate for the macroscopic crack driving force ( $K_I$ ) and Weibull stress values ( $\sigma_w$ ) for input to defect assessments under PTS conditions. This procedure becomes extraordinarily challenging and time consuming when assessments of vessel integrity need to be performed for a wide range of flaw sizes, shapes, locations, and orientations for ferritic steels with different elastic-plastic material properties under a large spectrum of thermal transients. The assessment procedure developed here for RPVs under PTS computes the cumulative probability of fracture essentially driven by the computed values of the scalar Weibull stress. The cumulative probability of failure ( $P_f$ ) remains unchanged if values of the scalar Weibull stress computed from a full 3-D model and from a simplified 2-D model (say, a SSY boundary layer model) for the same material flow property and crack-front loading condition (characterized, for example, by a two-parameter, crack-front stress field) have the same magnitude. One of the simplified assessment approaches, therefore, applies the  $K_I$ - $T$  values obtained from linear-elastic analyses of the 3-D embedded crack in an RPV, to a simplified 2-D, plane-strain SSY configuration, with the assumption

that the  $K_I$ - $T$  field in the 2-D SSY model replicates, with sufficient accuracy, the stress field near the front of the 3-D embedded crack in an RPV.

For ideal, well-contained plastic deformation near the crack front (without constraint loss,  $T_\sigma \geq 0$ ), the macroscopic crack driving force,  $K_I$ , fully characterizes the crack-front stress field. The Weibull stress values computed from a 2-D SSY model and from a 3-D fracture model (under high constraint), both subjected to an equivalent  $K_I$  field ( $T_\sigma = 0$ ), become identical. Under plane strain, SSY conditions, the non-zero  $T$ -stress characterizes the effect of geometry (specimen sizes, crack configurations, etc.) and loading mode (bending vs. tension) on the crack-front fields. Under SSY conditions, a negative  $T$ -stress quantifies the effect of constraint loss experienced in the crack-front field for real, 3-D flaws in an RPV. Therefore, the  $K_I$ - $T$  methodology (applied on a 2-D SSY model) can offer a simplified and realistic approximation of the stress fields near the front of the 3-D embedded crack in an RPV (with and without constraint loss) to compute Weibull stress values. Gao and Dodds [48] employ the  $K_I$ - $T$  methodology to assess the constraint effect on cleavage fracture specimens. Ongoing work [43] at ORNL also explores the feasibility of the 2-D  $K_I$ - $T$  approximation for embedded flaws in an RPV under PTS condition.

The essence of the  $K_I$ - $T$  approximation approach relies on the development of the relationship (or weight functions) between the Weibull stress value and values of the applied  $K_I$ - $T$  stresses on SSY configurations. This requires extensive analyses of the plane-strain SSY model with various  $K_I$ - $T$  displacement boundary conditions, including the temperature dependent material flow properties of various RPV materials. With  $\sigma_w$  represented by a comprehensive library of functions dependent on  $K_I$  and  $\beta$  ( $=T\sqrt{\pi a}/K_I$ ), the assessment procedure for RPVs under PTS simplifies into the following steps,

1. For a given RPV material, calibrate the temperature independent Weibull modulus ( $m$ ), using the procedure described in the Appendix. Compute values of  $\sigma_u$  and  $\sigma_{w-min}$  at selected, representative values of the temperature experienced along the crack front, at times of interest during a PTS event.
2. Perform a *linear-elastic* 3-D analysis of the flawed RPV. Compute the  $K_I$ - $T$  values along the embedded crack front for each time increment of the PTS transient. Divide the material near the crack front into  $n$  subregions. Each subregion experiences spatially constant values of temperature,  $K_I$  and  $T$ -stress. Use the  $\sigma_w$ -( $K_I$ ,  $\beta$ ) relationship developed from the 2-D SSY analyses to compute the Weibull stress value ( $\sigma_{w(i)}$ ) in each subregion, including proper thickness corrections (as outlined in the Appendix) for each subregion.
3. At the time of interest, insert the computed  $\sigma_{w(i)}$  and calibrated  $\sigma_{u(i)}$  and  $\sigma_{w-min(i)}$  values for each subregion along the crack front into Eq. 15 to compute the cumulative probability of failure ( $P_f$ ) for the embedded crack at that time during the PTS event.
4. Determine if SSY conditions remain in effect in the RPV for this level of loading through comparisons to fully 3-D, benchmark analyses.
5. Repeat step 3 for a new (increased) time during the PTS transient.

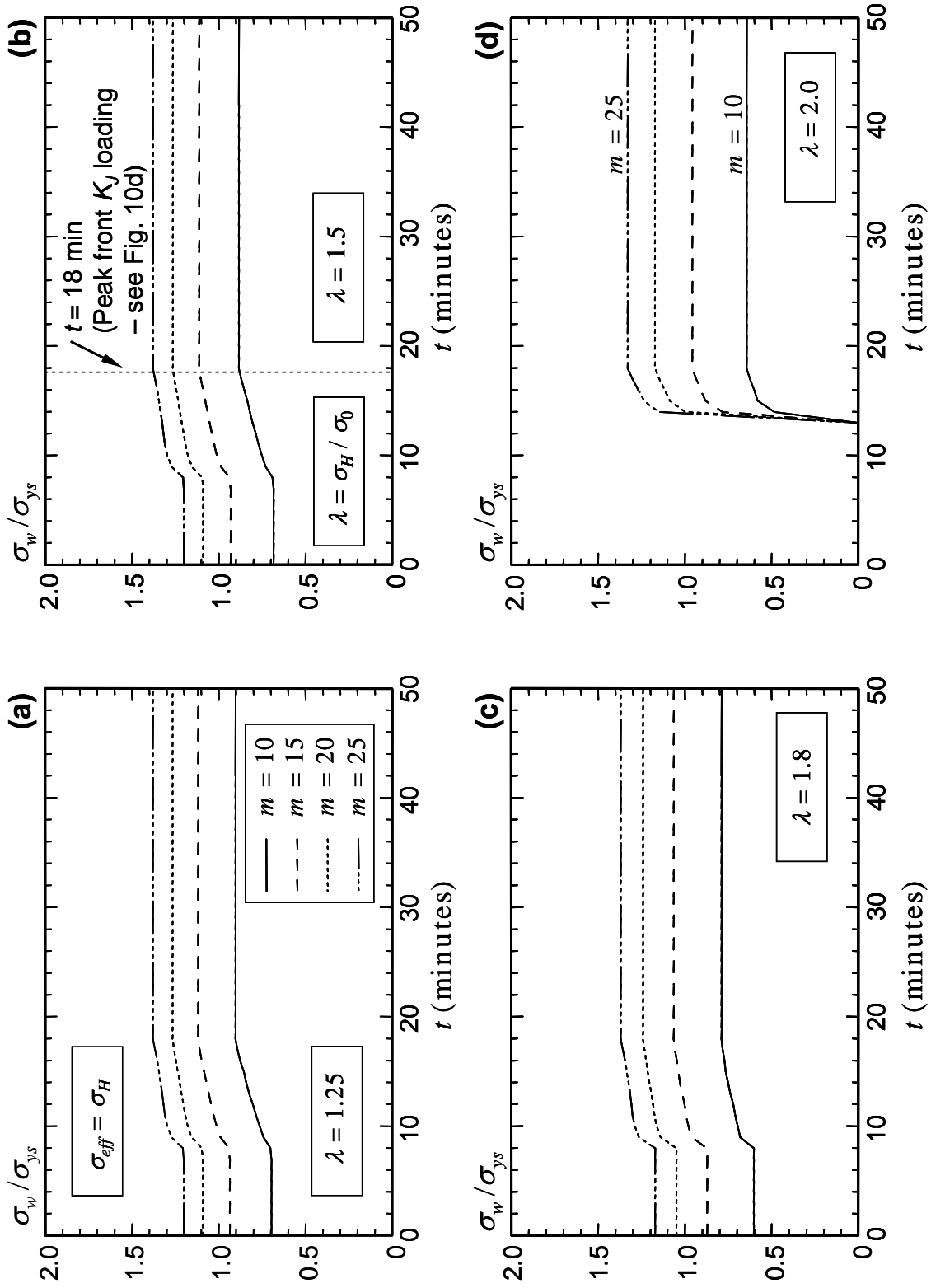


Fig. 14. Weibull stress variation over time history for an axially embedded flaw subjected to Transient A (20-node element model) with  $\sigma_{eff} = \sigma_H$  and: (a)  $\lambda = 1.25$ ; (b)  $\lambda = 1.5$ ; (c)  $\lambda = 1.8$ ; and (d)  $\lambda = 2.0$ .

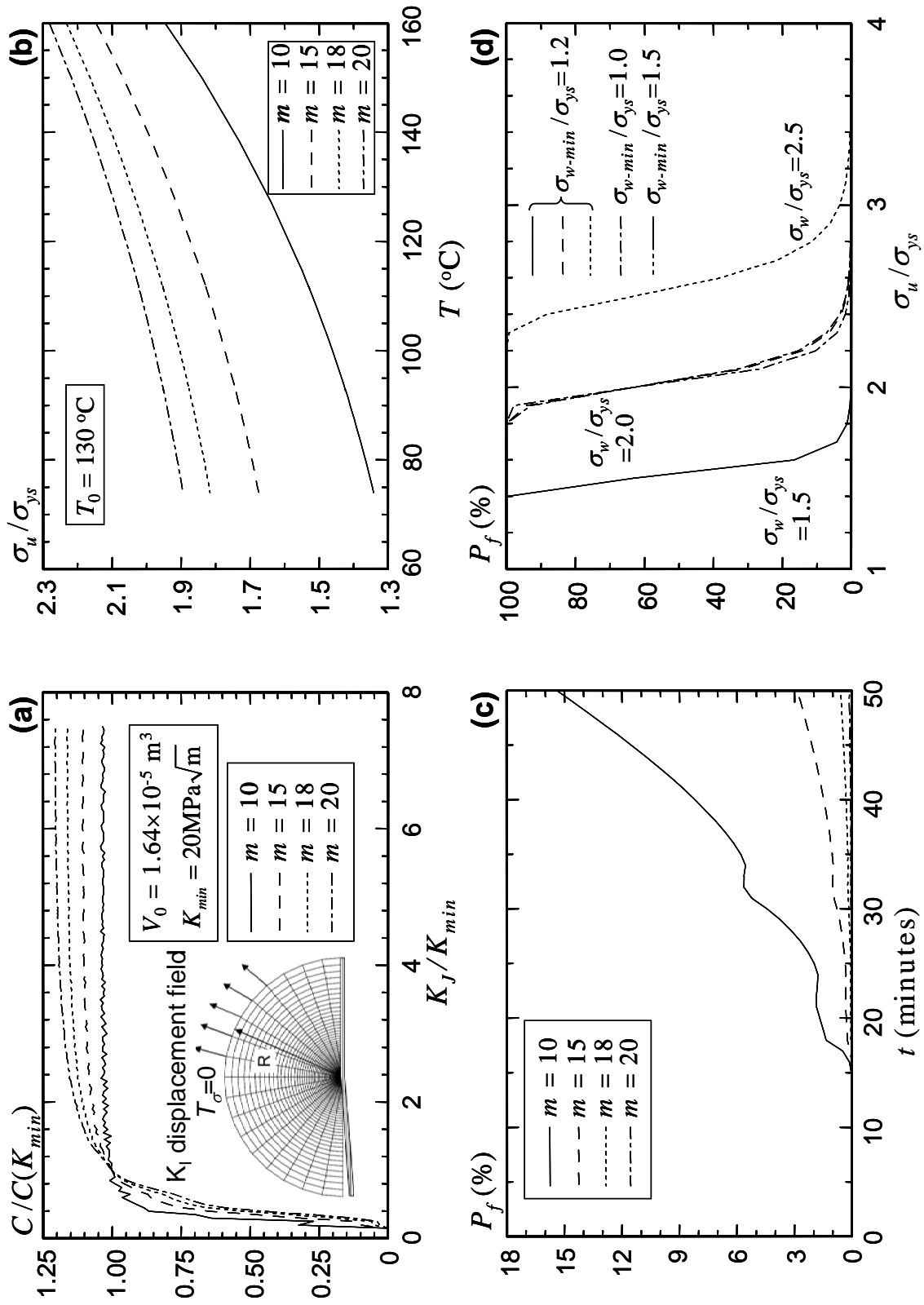


Fig. 15. (a) Evolution of constant  $C$  with  $K$ -values in SSY condition; (b) variation of (1T SSY)  $\sigma_u$  with respect to time at  $P_{crit}$  along the embedded crack front under Transient A; (c) cumulative probability of failure for the axial flaw under Transient A; and (d) sensitivity of  $P_f$  (computed from Eq. 12) to  $\sigma_u$ -values for fixed  $\sigma_w$  values.

This page is intentionally blank.

## 7 Summary and Conclusions

---

This study improves the understanding of failure assessment procedures for embedded cracks in RPVs under PTS events by (1) comparing the prediction of crack driving forces ( $K_J$ -values) via the conventional (LEFM) FAVOR code and the detailed, linear-elastic and elastic-plastic, 3-D finite element analyses, (2) computing the Weibull stress values along the full crack-front length of an embedded flaw, and (3) introducing details of three detailed assessment procedures based on the Weibull stress framework with an illustrative example. The selected RPV experiences two postulated transients: Transient A with a significant temperature gradient over the wall thickness coupled with a small change of the internal pressure and Transient B with a mild temperature gradient concurrent with significant repressurization. The detailed, 3-D thermal-mechanical analyses of RPVs conducted in this work investigate the effect of finite element types and models of material behavior on the magnitude of the macroscopic crack driving force ( $K_J$ ). The computation of Weibull stress values for the embedded crack front in an RPV demonstrates the influence of different effective stress definitions and values of the stress cutting parameter on the value of the scalar Weibull stress. The three proposed procedures for integrity assessments of RPVs include (1) a refined approach which considers the temperature dependent material flow and toughness properties along the crack front, (2) a simplified procedure which utilizes a spatially uniform, toughness value for the entire crack front, and (3) a  $K_J$ - $T$  methodology that approximates the 3-D crack-front fields through a linear-elastic,  $K_J$ - $T$  field on a 2-D, plane-strain SSY configuration.

The present work supports the following conclusions:

- (1) The 20-node element models provide more realistic  $K_J$ -values than the 8-node element models, which exhibit shear locking behavior under bending-type deformation caused by the thermal gradients across the wall thickness. Very detailed mesh refinement on the 8-node elements does not alleviate the shear locking phenomenon, and thus underestimates the  $K_J$ -values. The use of 8-node element models for PTS analyses of RPVs should be discontinued.
- (2) The 3-D linear-elastic (WARP3D) analysis predicts lower stress-intensity factors for embedded, elliptical flaws under PTS transients, compared to  $K_J$ -values computed from elastic-plastic (WARP3D) analyses. The elastic-plastic  $K_J$ -values are 20-30% higher than the linear-elastic SIFs for the axially embedded flaw under the examined Transients A and B. Similarly, the current version of the FAVOR code, which superimposes the mode I, stress-intensity-factor influence coefficients (weight functions) obtained from linear-elastic analyses, predicts lower stress-intensity factors than does the elastic-plastic analysis performed in WARP3D. FAVOR thus underpredicts the crack driving force values for the vessel geometries, crack sizes and loadings considered here.
- (3) The elastic-plastic analyses offer a more realistic description of the nonlinear behavior of material near the crack front. The actual, elastic-plastic material behavior redistributes the otherwise linear-elastic, asymptotic stresses near the crack front to adjacent material and increases the  $K_J$ -values, compared to linear-elastic SIF solutions. The mismatch in yield strengths of the cladding and base material also generates a potential influence on the nearby crack-front stress fields.
- (4) The unrealistic, high stress in the linear-elastic cladding shields the nearby base material between the nearest crack front and the base-cladding interface from significant plastic deformation. In contrast, the elastic-

plastic analyses includes the low yield stress of the cladding material, which redistributes stresses to the base material around the nearby crack front, and thus provides a more realistic and higher crack driving force ( $K_J$ ). The difference in the computed linear-elastic and elastic-plastic  $K_J$ -values are sufficient to cause non-trivial changes in the cumulative probability of failure. For example, the peak elastic-plastic stress-intensity values exceed the linear-elastic value by  $21 \text{ MPa}\sqrt{\text{m}}$  for the axially embedded flaw loaded by Transient A.

- (5) For the specific embedded circumferential and axial flaw configurations considered in this work, the axial flaw has much higher  $K_J$ -values along the crack front than the SIF solutions computed for the circumferential embedded flaw under the two transient loadings (for other crack sizes and locations through the vessel wall this observation may not hold). The remote (hoop) stress normal to the plane of the axially embedded flaw generated by the internal pressure equals approximately twice the (longitudinal) stress normal to the plane of the circumferentially embedded flaw. The axial flaw also resides nearer the inner surface of the RPV, and thus experiences lower temperatures than does the circumferential flaw. The size of the axially embedded flaw is also larger than the size of the circumferentially embedded flaw.
- (6) The Weibull stress values for the embedded flaw under PTS events depend significantly on the definition of the “effective” stresses. The Weibull stress computed using the hydrostatic stress,  $\sigma_H = (\sigma_1 + \sigma_2 + \sigma_3)/3$ , show 20-30% lower values than  $\sigma_w$ -values calculated using the maximum principal stress,  $\sigma_1$ . The effect of the stress cutting parameter,  $\lambda$ , on the computed Weibull stress value vanishes for high  $m$  values ( $\geq 13$ ), which promote the contribution of only the very highest stressed material to the Weibull stress.
- (7) The three proposed assessment procedures for embedded flaws under PTS conditions apply the Weibull stress framework (conventionally applied to straight, through-thickness cracks with uniform temperature) to the curved, embedded crack front with varying temperatures over the wall thickness of an RPV. The refined approach calibrates the temperature dependent material toughness properties in each of the  $n$  segments (“fracture specimens”) along the entire crack front and computes the cumulative probability of failure through Weibull stress values calculated in each segment with spatially constant temperature and  $K_J$ -values. The simplified approach applies the lowest toughness value (corresponding to the point with the lowest temperature along the front) to the entire crack front and computes the cumulative probability of failure through a Weibull stress value integrated (numerically) over the entire crack front. The  $K_J$ - $T$  methodology approximates the 3-D crack-front fields in an RPV via a simplified 2-D, plane-strain SSY configuration, linear-elastic  $K_I$ - $T$  fields. The Weibull stress values in different segments of the 3-D crack front therefore follows superposition of Weibull stress weight functions derived from the extensive 2-D SSY analyses. The cumulative probability of failure follows from the Weibull stress model (Eq. 12) including the temperature dependent material toughness properties along the crack front. Ongoing work will compare the applications of these three approaches.

## References

---

1. Li F. Assessment of pressure vessel failure due to pressurized thermal shock with consideration of probabilistic-deterministic screening and uncertainty analysis, Ph.D. Dissertation, Center for Technology Risk Studies, University of Maryland, 2001.
2. Fang T, Modarres M. Probabilistic and deterministic treatments for multiple flaws in reactor pressure vessel safety analysis. Trans 17<sup>th</sup> Inter Conf Struct Mech Reactor Tech 2003.
3. Buchalet CB, Bamford WH. Stress intensity factor solutions for continuous surface flaws in reactor pressure vessels. ASTM STP 590 1976;385-402.
4. McGowan JJ, Raymund M. Stress intensity factor solutions for internal longitudinal semi-elliptical surface flaws in a cylinder under arbitrary loadings. ASTM STP 677 1979;365-380.
5. Raju IS, Newman JC Jr. Stress intensity factor influence coefficients for internal and external surface cracks in cylindrical vessels. PVP Vol 58. Aspects of Fracture Mechanics in Pressure Vessels and Piping 1982; 37-48.
6. Bryson JW, Dickson TL. Stress-intensity-factor influence coefficients for axial and circumferential flaws in reactor pressure vessels. PVP Vol. 250. ASME Pres Ves Piping Conf 1993;77-88.
7. Bryson JW, Dickson TL. Stress-intensity-factor coefficients for circumferentially oriented semielliptical inner surface flaws in clad pressure vessels ( $R_i/t = 10$ ). ORNL/NRC/LTR-94/8, Oak Ridge National Laboratory, Oak Ridge, TN, Apr, 1994.
8. Dickson TL, Keeney JA, Bryson JW. Validation of FAVOR code linear-elastic fracture solutions for finite-length flaw geometries. PVP Vol. 304. Fatigue and Fracture Mechanics in Pressure Vessels and Piping. ASME Pres Ves Piping Conf 1995;51-58.
9. Dickson TL, Bass BR, Williams PT. Validation of a linear-elastic fracture methodology for postulated flaws embedded in the wall of a nuclear reactor pressure vessel. PVP Vol. 403. Severe Accidents and other topics in RPV design. ASME Pres Ves Piping Conf 2000;145-151.
10. Williams PT, Dickson TL, Yin S. Fracture analysis of vessels-Oak Ridge FAVOR, v04.1, computer code: theory and implementation of algorithms, methods, and correlations. NUREG/CR-6854. 2004.
11. Williams PT, Dickson TL, Yin S. Fracture analysis of vessels-Oak Ridge FAVOR, v04.1, computer code: user's guide. NUREG/CR-6855. 2004.
12. Wallin K. The scatter in  $K_{Ic}$ -results. Engng Fract Mech 1984;19:1085-1093.
13. Batdorf SB, Crose JG. A statistical theory for the fracture of brittle structures subjected to non-uniform polyaxial stresses. J App Mech 1974;41:459-464.

14. Evans AG. A general approach for the statistical analysis of multiaxial fracture. *J Amer Ceramic Soc* 1978;61:302-308.
15. Matsuo Y. Statistical theory for multiaxial stress states using Weibull's three-parameter function. *Engng Fract Mech* 1981;14:527-538.
16. Beremin FM. A local criterion for cleavage fracture of a nuclear pressure vessel steel. *Metallur Trans* 1983;14A:2277-2287.
17. Mudry F. A local approach to cleavage fracture. *Nucl Engng Des* 1987;105:65-76.
18. Griffith AA. The phenomena of rupture and flow in solids. *Phil Trans* 1920;221:A:163-198.
19. Lidbury DPG, Bass BR, Bhandari S, Sherry AH. Key features arising from structural analysis of the NESC-1 PTS benchmark experiment. *Int J Pres Ves Piping* 2001;78:225-236.
20. Bernauer G, Brocks W, Schmitt W. Modifications of the Beremin model for cleavage fracture in the transition region of a ferritic steel. *Engng Fract Mech* 1999;64:305-325.
21. Gao X, Ruggieri C, Dodds RH Jr. Calibration of Weibull stress parameters using fracture toughness data. *Int J Fract* 1998;92:175-200.
22. El-Shennawy M, Minami F, Toyoda M, Kajimoto K. Crack-tip constraint activators and the application to plane-strain fracture toughness test: Proposal on small-size fracture toughness specimen. *Engng Fract Mech* 1999;63: 447-479.
23. Ruggieri C, Dodds RH Jr. Numerical evaluation of probabilistic fracture parameters with WSTRESS. *Engng Comp* 1998;15:49:73.
24. Minami F, Bruckner-Foit A, Munz D, Trolldenier B. Estimation procedure for the Weibull parameters used in the local approach. *Int J Fract* 1992;54:197-210.
25. Gao X, Dodds RH Jr. Constraint effects on the ductile-to-brittle transitions temperature of ferritic steels: a Weibull stress model. *Int J Fract* 2000;102:43-69.
26. Ruggieri C, Dodds RH Jr. Probabilistic modeling of brittle fracture including 3-D effects on constraint loss and ductile tearing. *J Phys IV* 1996;6:C6:353-62.
27. Petti JP, Dodds RH Jr. Constraint comparisons for common fracture specimens: C(T)s and SE(B)s. *Engng Fract Mech* 2002; 71:2677-2683.
28. Petti JP, Dodds RH Jr. Coupling of the Weibull stress model and macroscale models to predict cleavage fracture. *Engng Fract Mech* 2004;71:2079:2103.
29. Test method for the determination of reference temperature  $T_0$  for ferritic steels in the transition range (ASTM E1921), American Society for Testing and Materials, 2002, Philadelphia.

30. Lee BS, Hong JH, Yang WJ, Huh MY, Chi SH. Master Curve characterization of the fracture toughness in unirradiated RPV steels using full- and 1/3-size pre-cracked Charpy specimens. *Int J Pres Vess Piping* 2000;77:599-604.
31. Server W, Rosinski S, Lott R, Kim C, Weakland D. Application of Master Curve fracture toughness for reactor pressure vessel integrity assessment in the USA. *Int J Press Ves Piping* 2002;79:701-713.
32. Margolin BZ, Shvetsova VA, Gylenko AG, Ilyin AV, Nikolaev VA, Smirnov VI. Fracture toughness predictions for a reactor pressure vessel steel in the initial and highly embrittled states with the Master Curve approach and a probabilistic model. *Int J Pres Ves Piping* 2002;79:219-231.
33. Moinereau D, Bezdikian G, Faigy C. Methodology for the pressurized thermal shock evaluation: recent improvements in French RPV PTS assessment. *Int J Pres Ves Piping* 2001;78:69-83.
34. Comparison report of RPV pressurized thermal shock international comparative assessment study (PTS ICAS). NEA/CSNI/R(99)3, OECD Publications, Paris, France, 1999.
35. Kirk M, Mitchell M. Potential roles for the Master Curve in regulatory application. *Int J Pres Ves Piping* 2001;78:111-123.
36. Gullerud A, Koppenhoefer K, Roy A, RoyChowdhury S, Walters M, Bichon B, Cochran K, Carlyle A, Dodds RH Jr. WARP3D: 3-D dynamic nonlinear fracture analysis of solids using parallel computers and workstations. Structural Research Series (SRS) 607, UILU-ENG-95-2012, 2006, University of Illinois at Urbana-Champaign.
37. Wallin K, Saario T, Torronen K. Statistical model for carbide induced brittle fracture in steel. *Metal Science* 1984;18:13-16.
38. Lin T, Evan AG, Ritchie RO. A statistical model of brittle fracture by transgranular cleavage. *J Mech Phys Solids* 1986;21:263-277.
39. Petti JP, Dodds RH Jr. Calibration of the Weibull stress scale parameter,  $\sigma_u$ , using the Master Curve. *Engng Fract Mech* 2005;72:91-120.
40. Wasiluk B, Petti JP, Dodds RH Jr. Temperature dependence of Weibull stress parameters: studies using Euro-material similar to ASME A508 Class-3 steel. NUREG/CR-6930. 2007.
41. Heerens J, Hellmann D. Development of the Euro fracture toughness dataset. *Engng Fract Mech* 2002;69:421-449.
42. Wallin K. Master curve analysis of the Euro fracture toughness dataset. *Engng Fract Mech* 2002;69:451-481
43. Yin S, Bass BR, Williams PT, Dickson TL. Develop benchmark problem for  $T$ -stress assessment of embedded flaw. ORNL Report, 2005.

44. Arcieri WC, Beaton RM, Fletcher CD, Bessette DE. RELAP5 thermal hydraulic analysis to support PTS evaluation for the Oconee-1, Beaver Valley-1, and Palisades nuclear power plants. NUREG/CR-6858. 2004.
45. Structural Reliability Technology. FEACrack: 3-D finite element software for cracks, version 2.7: user's manual. <http://www.srt-boulder.com>. 2005.
46. Ruggieri C, Gao X, Dodds RH Jr. Transferability of elastic-plastic fracture toughness using the Weibull stress approach: significance of parameter calibration. *Engng Fract Mech* 2000;67:101-117.
47. Williams PT, Bass BR, McAfee WJ. Shallow flaws under biaxial loading conditions, part II: application of the Weibull stress analysis of the cruciform bend specimen using a hydrostatic stress criterion. *J Press Ves Tech* 2001;123:25-31.
48. Gao X, Dodds RH Jr. An engineering approach to assess constraint effects on cleavage fracture toughness. *Engng Fract Mech* 2001;68:263-268.
49. Boley, BA, Weiner, JH. *Theory of Thermal Stresses*. John Wiley & Sons, Inc; 1960.

## Appendix A: Calibration of Weibull Stress Model

---

The calibration procedure for the unique, temperature invariant Weibull modulus,  $m$ , utilizes the constraint difference between two different sets of fracture toughness values measured at a common temperature — one set measured using high constraint specimens and one set measured using low constraint specimens. The low constraint specimens fracture at crack-front conditions characterized by at least two independent parameters (*i.e.*, the  $K$ - $T$  field or the  $J$ - $Q$  field) which enable calibration for a unique pair ( $m$ ,  $\sigma_u$ ). The calibration procedure uses trial values of  $m$  to scale (constraint correct) each set of toughness values to a common reference configuration (typically 1T plane-strain, small scale yielding condition with zero  $T$ -stress), through the following equation,

$$K_{Jc}^{SSY(1T)} = K_{min} + \left[ g\left(M^{(xT)}\right)^{1/4} K_{Jc}^{(xT)} - g\left(M_{min}^{(xT)}\right)^{1/4} K_{min} \right] \left[ \frac{B_{xT}}{B_{1T}} \right]^{1/4}, \quad (A1)$$

where the  $g(M^{(xT)})$  function characterizes the level of constraint difference between the ideal, plane-strain 1T SSY condition (with zero  $T$ -stress) and a specific fracture specimen with a thickness of  $xT$ . The  $g(M_{min}^{(xT)})$  term in Eq. A1 defines the constraint difference corresponding to the far field crack driving force  $K = K_{min}$ , and equals 1.0 for common test specimen sizes (1T) which experiences no constraint loss at  $K = K_{min}$ . The  $g(M)$  function derives from the (constraint) difference reflected by the  $\sigma_w$  -  $K_J$  relationship computed from the 3-D, nonlinear finite element analysis for a plane-strain, SSY boundary-layer model and that for a specific fracture specimen, as described by,

$$\sigma_w^m = CBK_{J(avg)}^4 g(M), \quad (A2)$$

where  $M = b\sigma_0 / J_{avg}$  and  $J_{avg}$  denotes a through-thickness average value. The parameters  $b$  and  $B$  define the ligament length and the thickness of the specimen, respectively. The constraint function,  $g(M)$ , equals 1.0 for all materials under plane-strain, SSY condition with zero  $T$ -stress. The coefficient  $C$  refers to a constant dependent on the material flow properties, temperature and Weibull stress parameters ( $m$  and  $V_0$ ). The value of the coefficient  $C$  follows from the  $\sigma_w$  -  $K_J$  solution for a plane-strain, SSY reference configuration ( $T_\sigma = 0$ ) with  $g(M) = 1$  in Eq. A2. (Equation A2 also provides the thickness correction scheme for SSY models [ $g(M) = 1$ ] with different thickness,  $B$ , subjected to the same, remote  $K_I$  -  $T$  field.)

Wasiluk *et al.* [43] employ an updated version of the least square procedure to calibrate the Weibull modulus,  $m$ . The error measure applies a weight factor to each measured toughness value designed to reduce the relative contribution of experimental values with the largest uncertainty in failure probability.

The following steps describe the calibration procedure:

1. Test two sets of specimens at the same temperature in the DBT region that have markedly different constraint:
  - high constraint (HC) data set, with  $n_{HC}$  specimens, that approaches small-scale yielding conditions, having  $M \geq 100$ ,
  - a low constraint (LC) data set, with  $n_{LC}$  specimens, under large-scale yielding but without significant ductile tearing prior to cleavage fracture in each specimen.

The subsequently calibrated parameters for the Weibull stress model then apply strictly for the test temperature.

2. Obtain uniaxial, (true) stress-strain curve for the test temperature to strain values of  $\approx 2.0$  (needed for ensuring accuracy in the finite element analysis)
3. For the purposes of data visualization, rank order each of the experimental data sets and calculate the rank probability of failure for each specimen in each data set,

$$P_{i-\text{rank}}^{\text{LC}} = \frac{i-0.3}{n_{\text{LC}}+0.4}, P_{i-\text{rank}}^{\text{HC}} = \frac{i-0.3}{n_{\text{HC}}+0.4}, \quad (\text{A3})$$

where  $n_{\text{HC}}$  and  $n_{\text{LC}}$  denote the number of specimens in each data set and  $i$  refers to the rank number, respectively.

4. Perform nonlinear 3-D finite element analyses as described in [43] for:
  - Both HC and LC test specimen geometries, and
  - The plane-strain reference configuration, 1T SSY (zero  $T$ -stress),

The stored, stress-strain results for each element at each analysis load step enable very rapid computation of the Weibull stress value using Eq. 10 for a specified, trial value of  $m$ .

5. Assume trial values for  $m$  and  $K_{\min}$  (or fix  $K_{\min}$  at  $20 \text{ MPa} \sqrt{\text{m}}$  as in E1921). From 3-D finite element results, compute the evolution of  $\sigma_w$  vs.  $J$  for the specimens (HC and LC) and for the 1T SSY reference condition. Convert  $J$ -values to  $K_J$ -values by applying the plane-strain conversion (the calibration process is expressed in terms of  $K_J$  to maintain similarity with E1921 terminology). Set the value of  $\sigma_{w-\min} = \sigma_w(K_J = K_{\min})$ .
6. Correct the high and low constraint toughness values to the 1T SSY plane-strain condition using Eq. A1. This yields two sets of toughness values termed  $K_{Jc}^{\text{HC-1T SSY}}$  and  $K_{Jc}^{\text{LC-1T SSY}}$ , or generally as  $K_{Jc}^{\text{xC-1T SSY}}$ .
7. Compute  $K_0^{\text{HC-1T SSY}}$  for the high constraint data set, using the maximum likelihood method which yields,

$$K_0^{\text{HC-1T SSY}} = \left[ \sum_{i=1}^{n_{\text{HC}}} \frac{\left( K_{Jc(i)}^{\text{HC-1T SSY}} - K_{\min} \right)^4}{(r-0.3068)} \right]^{1/4} + K_{\min}. \quad (\text{A4})$$

Use  $K_0^{\text{HC-1T SSY}}$  and trial values of  $K_{\min}$  to define a continuous, cumulative failure probability function termed here  $K_{Jc}^{\text{1T SSY}}$  from,

$$P_f \left( K_{Jc}^{\text{1T SSY}} \right) = 1 - \exp \left[ - \left( \frac{K_{Jc}^{\text{1T SSY}} - K_{\min}}{K_0^{\text{HC-1T SSY}} - K_{\min}} \right)^4 \right]. \quad (\text{A5})$$

8. For the trial pair  $m$  and  $K_{\min}$ , calculate a scalar error measure to characterize differences between the HC and LC constraint corrected distributions. The new error measure here includes two parts: (1) the summed differences between the high and low constraint corrected data sets (step 6) and the continuous SSY distribution (step 7); and (2) the summed differences between the  $K_{Jc}$ -values for the high and low constraint data sets scaled to SSY (both from step 6).

$$\text{Error}(m, K_{\min}) = \sum_{i=1}^{n_{\text{HC}}+n_{\text{LC}}} \left| K_{Jc}^{\text{xC-1T SSY}} - K_{Jc}^{\text{1T SSY}} \right| WF_{(i)} + \sum_{i=1}^{n_{\text{HC}}+n_{\text{LC}}} \left| K_{Jc}^{\text{HC-1T SSY}} - K_{Jc}^{\text{LC-1T SSY}} \right| WF_{(i)}. \quad (\text{A6})$$

The multiplier,  $WF$ , denotes a weight function factor ( $\sum WF \equiv 1$ ), which scales the error contribution for a given value of  $i$  based on the confidence in the current failure probability. Wasiluk *et al.* [43] provide a detailed description of the weight function and include modifications to handle the case with  $n_{HC} \neq n_{LC}$ .

Other, similar error measures likely would lead to equally satisfactory estimates for the parameters.

9. Repeat steps 5-8 for additional trial values of  $m$  and  $K_{min}$ .
10. The calibrated pair  $(m, K_{min})$  minimizes the error function (no convergence criterion is required).

After calibration of  $m$  and  $K_{min}$ , compute values for  $\sigma_u$  and  $\sigma_{w-min}$  using the finite element results for  $\sigma_w$  vs.  $J$ , with  $\sigma_u^{1T SSY} = \sigma_w(K_J = K_0^{1T SSY})$  and  $\sigma_{w-min}^{1T SSY} = \sigma_w(K_J = K_{min})$ . The following equation scales the calibrated  $\sigma_u^{1T SSY}$  to the experimental specimen configuration ( $xTxC$ ),

$$\sigma_u^{xTxC} = 4/m \sqrt{\sigma_u^{m/4} \Big|^{1T SSY} - \sigma_{w-min}^{m/4} \Big|^{1T SSY} + \sigma_{w-min}^{m/4} \Big|^{xTxC}} \quad (A7)$$

where  $\sigma_{w-min}^{xTxC}$  denotes the  $\sigma_w$  value corresponding to  $K_J = K_{min}$  for the  $xT$  size specimen of interest. The value of  $\sigma_{w-min}^{xTxC}$  derives from Eq. A2, with  $g(M) = 1.0$  for specimens without constraint loss at  $K_{min}$ . Using  $m$ ,  $\sigma_u^{xTxC}$ , and  $\sigma_{w-min}^{xTxC}$ , predictions of the cumulative probability of failure for the  $xT$  size specimen at a given temperature follow from Eq. 12.

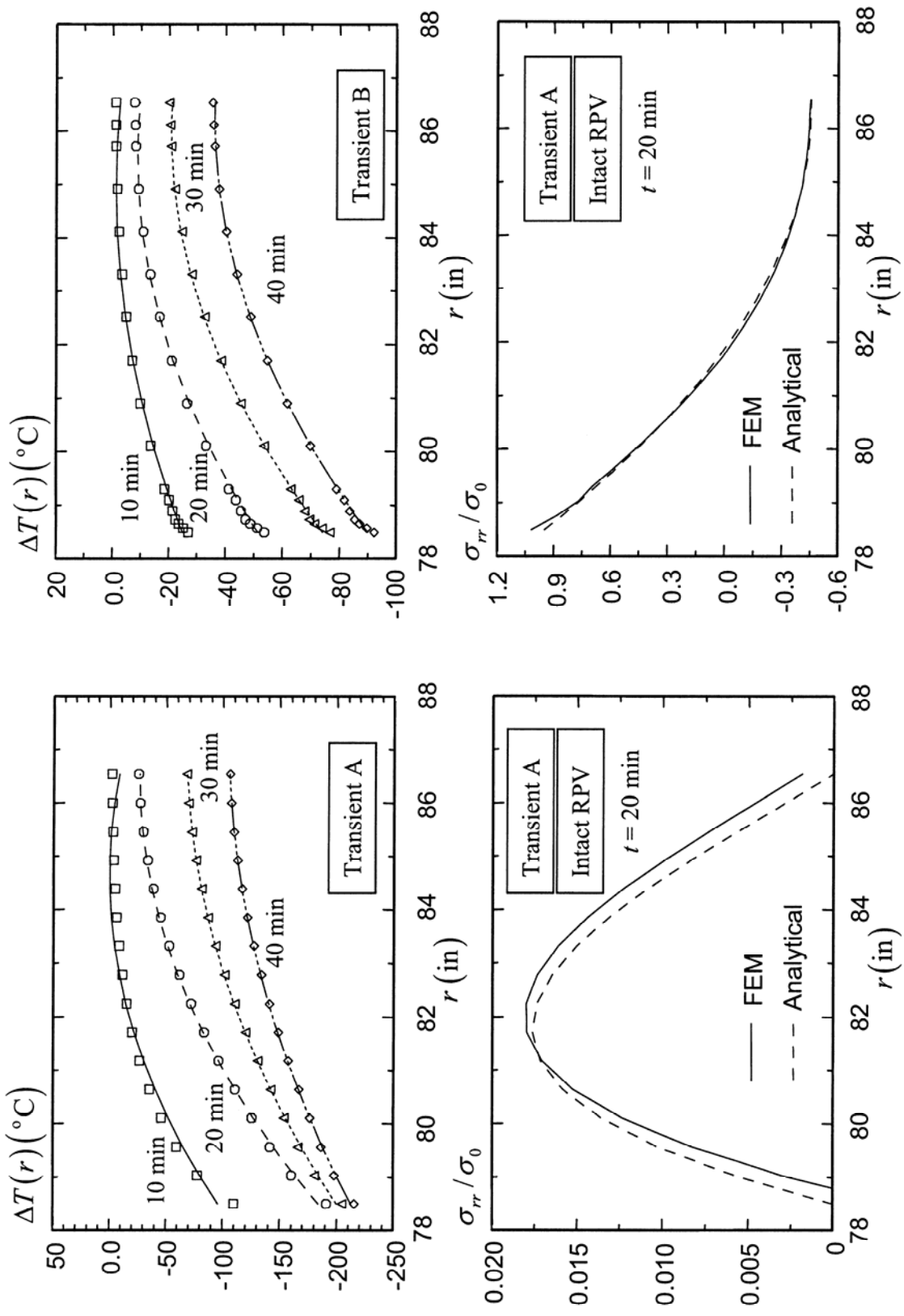


Fig. A1. Quadratic approximation of temperature variations over the wall thickness of an RPV under (a) transient A and (b) transient B. Comparison of the analytical solution and the FE analysis over the wall thickness of an RPV at  $t = 20$  min of transient A for (c)  $\sigma_{rr}$  and (d)  $\sigma_{\theta\theta}$ .

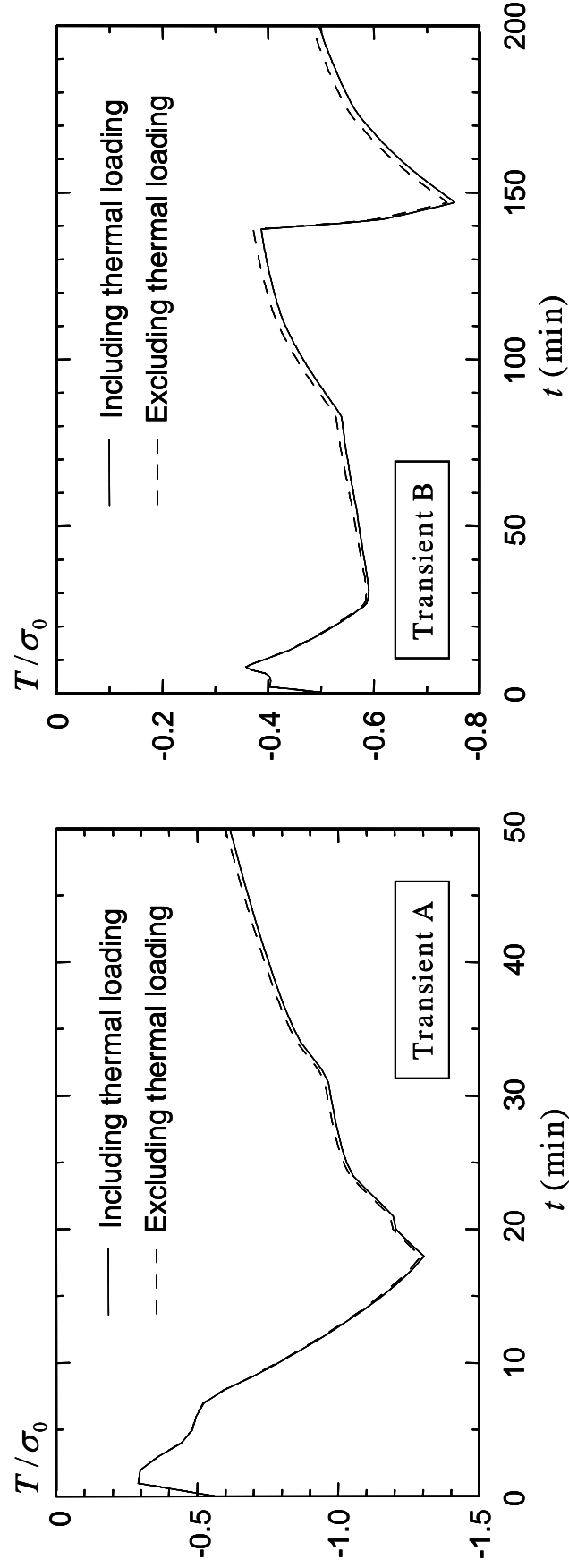


Fig. A2. Comparison of the  $T$ -stress values computed using the interaction integral including thermal loadings and that excluding thermal loadings for an RPV under (a) transient A; and (b) transient B.

This page is intentionally blank.

## Appendix B: Future Work

---

The current study develops simplified and refined procedures for failure assessments of RPVs under PTS events, based on detailed, elastic-plastic finite element investigations of an RPV under two postulated transients. The computation of the cumulative probability of fracture for an embedded flaw under a PTS transient employs the Weibull stress framework using the model parameters calibrated from approaches proposed by previous researchers [28, 42, 43]. With the current (elastic-plastic) benchmark studies, future research efforts aim to develop computationally more tractable approaches, incorporating the following tasks:

1. Implement, through an independent (FORTRAN) code, the proposed, refined procedure to compute the cumulative probability of fracture for the entire front of an embedded flaw in an RPV under a PTS transient. The FORTRAN program will divide the curved crack front into multiple segments with spatially constant  $K_I$  - values and spatially constant temperatures, and compute the  $\sigma_{w(i)}$  -values independently for each segment. The total cumulative probability of failure for the entire crack front follows Eq. 15, with temperature dependent Weibull scale parameter,  $\sigma_{u(i)}$ , and the Weibull threshold value,  $\sigma_{w-min(i)}$ , calibrated for each segment. The difference in the cumulative probability of failure computed from this refined approach and that computed from the current simplified approach indicate the amount of conservatism offered by the simplified approach in the failure assessment procedure.
2. Examine the feasibility and applicability of the  $K_I$  - $T$  methodology in approximating the Weibull stress values for the full 3-D crack front in an RPV through a 2D, plane-strain SSY model driven by the linear-elastic  $K_I$  - $T$  field obtained from the 3-D RPV model. This work will assess the effect of  $T$ -stresses on the Weibull stress values using the SSY configuration. For applications of the  $K_I$  - $T$  methodology to RPVs under PTS events, the failure assessment procedure first computes the  $K_I$  - $T$  values in each crack-front segment of the embedded flaw. The elastic-plastic analyses of the SSY model under the corresponding set of  $K_I$  - $T$  values yield the Weibull stress values in each segment along the crack front. The total cumulative probability of failure (from Eq. 15), incorporating the temperature dependent Weibull stress parameters, represents a simplified but detailed failure assessment approach.
3. Apply the Weibull methodology to the biaxial cruciform EURO data generated by ORNL for the VOCALIST project [55]. The VOCALIST project [55] includes independent calibration of the Weibull stress parameters by different participating organizations, which demonstrate significant variance in the Weibull modulus,  $m$ , for different calibration schemes. Further investigation will focus on developing a standard procedure for application of the Weibull calibration methodology to cleavage fracture of RPV materials.

This page is intentionally blank.

## Appendix C: Analytical Solution for Thermal Induced T-stress

This section describes the analytical solution for the radial stress,  $\sigma_{rr}$ , derived for a very long cylinder under temperature variation over the wall thickness in the absence of mechanical loadings, using a 2-D, plane-strain mathematical model. The plane-strain condition approximates the condition for the RPV material near the symmetry plane at  $y=0$  (see Fig. 1). For either an axially embedded or a circumferentially embedded flaw in an RPV, the thermal induced  $T$ -stress for the crack-front region near symmetry plane ( $y=0$ ) depends solely on  $\sigma_{rr}$ .

The analytical solution adopts the following assumptions. The temperature variation,  $\Delta T(r)$ , depends on the radius only. The displacement along the circumferential direction,  $u_\theta$ , equals zero. The stress, strain, displacement field variables remain constant with respect to the variation in  $\theta$ . The material properties of the RPV employ a homogeneous base material and neglect the mismatches in the mechanical and thermal properties between the base and cladding steels. The loading condition of the RPV includes thermal loadings only, and assumes zero internal pressure and body forces.

Boley *et al.* [49] show that the plane-strain, stress solutions for a very long cylinder under temperature variation over the wall thickness follow,

$$\sigma_{rr} = -\frac{\alpha' E'}{r^2} \int_{r_i}^r \Delta T r dr + \frac{E' C_1}{1-\nu'} - \frac{E' C_2}{(1+\nu') r^2}, \quad (C1)$$

$$\sigma_{\theta\theta} = \frac{\alpha' E'}{r^2} \int_{r_i}^r \Delta T r dr - \alpha' E' T + \frac{E' C_1}{1-\nu'} + \frac{E' C_2}{(1+\nu') r^2}, \quad (C2)$$

where  $E' = E/(1-\nu^2)$ ,  $\nu' = \nu/(1-\nu)$ , and  $\alpha' = \alpha(1+\nu)$ .  $r_i$  and  $r_o$  refer to the inner and outer radius of the RPV respectively.  $C_1$  and  $C_2$  are constants depending on the following boundary conditions,

$$\sigma_{rr}(r=r_i) = \sigma_{rr}(r=r_o) = 0, \quad (C3)$$

For a constant temperature variation over the wall thickness,

$$\sigma_{rr} = \sigma_{\theta\theta} = 0. \quad (C4)$$

For a linear temperature variation over the wall thickness,

$$\Delta T = ar + b, \quad (C5)$$

the radial and circumferential stresses become,

$$\sigma_{rr} = \frac{\alpha' E' a}{3} \left[ \frac{r^2 - r_i^2}{r^2} \frac{r_o^2 + r_i r_o + r_o^2}{r_o + r_i} - \frac{r^3 - r_i^3}{r^2} \right], \quad (C6)$$

$$\sigma_{\theta\theta} = \frac{\alpha' E' a}{3} \left[ \frac{r^2 + r_i^2}{r^2} \frac{r_o^2 + r_i r_o + r_o^2}{r_o + r_i} - \frac{r_i^3}{r^2} \right]. \quad (C7)$$

For a quadratic temperature variation over the wall thickness,

$$\Delta T = ar^2 + br + c, \quad (C8)$$

the radial and circumferential stresses follow from,

$$\sigma_{rr} = -\frac{\alpha' E'}{r^2} \left[ \frac{a}{4}(r^4 - r_i^4) + \frac{b}{3}(r^3 - r_i^3) + \frac{c}{2}(r^2 - r_i^2) \right] + \alpha' E' \left( 1 - \frac{r_i^2}{r^2} \right) \left[ \frac{a}{4}(r_i^2 + r_o^2) + \frac{b}{3} \frac{r_i^2 + r_i r_o + r_o^2}{r_i + r_o} + \frac{c}{2} \right], \quad (C9)$$

$$\sigma_{\theta\theta} = \frac{\alpha' E'}{r^2} \left[ \frac{a}{4}(r^4 - r_i^4) + \frac{b}{3}(r^3 - r_i^3) + \frac{c}{2}(r^2 - r_i^2) \right] - \alpha' E' (ar^2 + br + c) + \alpha' E' \left( 1 + \frac{r_i^2}{r^2} \right) \left[ \frac{a}{4}(r_i^2 + r_o^2) + \frac{b}{3} \frac{r_i^2 + r_i r_o + r_o^2}{r_i + r_o} + \frac{c}{2} \right]. \quad (C10)$$

Figures A1a and A1b illustrate the quadratic approximation of the temperature variation over the wall thickness for transients A and B considered in the current study. The analytical stress solutions computed from Eqs. C9 and C10 demonstrate close agreement with the stress values computed from an FE analysis for the intact RPV under transient A at  $t = 20$  min. The very small value of  $\sigma_{rr}$  indicates negligible  $T$ -stresses for the nearby crack front generated by a quadratic temperature variation over the wall thickness. Figure A2 compares the  $T$ -stress values (at point B in Fig. 9) for the RPV under both transients computed using the interaction integral approach including the thermal loading and that excluding the thermal loading. The close agreement between  $T$ -stress values computed using these two approaches demonstrate that the  $T$ -stress for an axial or a circumferential flaw near the symmetry plane ( $y = 0$ ) in an RPV derives mainly from the mechanical loading (internal pressure).